

Implicit Neural Networks with Fourier-Feature Inputs for Free-breathing Cardiac MRI Reconstruction

Johannes F. Kunz*, Stefan Ruschke[†], Reinhard Heckel*

*Dept. of Electrical and Computer Engineering, Technical University of Munich

[†] Dept. of Diagnostic and Interventional Radiology, Klinikum rechts der Isar,
School of Medicine, Technical University of Munich

May 12, 2023

Abstract

In this paper, we propose an approach for cardiac magnetic resonance imaging (MRI), which aims to reconstruct a real-time video of a beating heart from continuous highly under-sampled measurements. This task is challenging since the object to be reconstructed (the heart) is continuously changing during signal acquisition. To address this challenge, we represent the beating heart with an implicit neural network and fit the network so that the representation of the heart is consistent with the measurements. The network in the form of a multi-layer perceptron with Fourier-feature inputs acts as an effective signal prior and enables adjusting the regularization strength in both the spatial and temporal dimensions of the signal. We examine the proposed approach for 2D free-breathing cardiac real-time MRI in different operating regimes, i.e., for different image resolutions, slice thicknesses, and acquisition lengths. Our method achieves reconstruction quality on par with or slightly better than state-of-the-art untrained convolutional neural networks and superior image quality compared to a recent method that fits an implicit representation directly to Fourier-domain measurements. However, this comes at a higher computational cost. Our approach does not require any additional patient data or biosensors including electrocardiography, making it potentially applicable in a wide range of clinical scenarios.

1 Introduction

Real-time magnetic resonance imaging (MRI) is a dynamic imaging technique for assessing the anatomic structure and function of moving organs in the human body. The reconstruction of cardiac function is challenging due to the relatively fast organ movements compared to the achievable encoding speed. In this paper, we consider the reconstruction of free-breathing cardiac real-time MRI data, where the goal is to reconstruct a video of the beating heart from highly under-sampled data continuously acquired over multiple cardiac and respiratory cycles. The video depicts the cardiac function in real-time meaning that arrhythmia and unprecedented motion can be imaged without assuming periodicity of the motion. This task is especially difficult when only very few samples are collected at any given time instance during the cardiac and respiratory cycles.

Various reconstruction methods for cardiac MRI are based on gated or triggered data [Lan+84; Lar+04]. Such methods bin the measurements according to different times in the cardiac and respiratory cycle. The bins are then reconstructed independently using methods for static MRI, or they are reconstructed jointly using signal priors for regularizing among bins [Fen+16; Chr+18; Jia+18]. However, binning can lead to artifacts since the heart may not be exactly in the same position at a given point in the cardiac and respiratory cycle, and periodicity of the motion needs to be assumed.

Another class of methods does not rely on gating or triggering, but reconstructs images from continuously acquired un-gated data by regularizing in the spatial and temporal dimensions with hand-crafted signal priors, for example with total-variation norm penalties [Fen+14] and through imposing low-rank priors [Ong+20; Nak+17; Pod+19; Pod+19]. Thereby, the heart can be imaged in real-time without binning-related inaccuracies.

With the advent of deep learning, signal priors can be learned from data. Supervised methods have been proposed for dynamic MRI that are trained on pairs of measurement data and corresponding ground-truth images [Sch+18; Qin+19; K  s+20; Hua+21]. However, ground-truth fully sampled images are generally not available for real-time MRI without assuming periodicity of the motion.

A recent elegant approach to avoid the use of training data but benefit from the prior inherent in neural networks are untrained networks that regularize by fitting a neural network to the measurement data. Untrained neural networks are typically based on convolutional neural networks (CNNs) [Yoo+21; Zou+21; Ahm+22; BAJ19], since CNNs have a provable bias towards fitting smooth signals [HS20b; HS20a].

In this paper, we propose an untrained approach for cardiac real-time MRI that is based on representing the beating heart with a multi-layer perceptron (MLP) with Fourier-feature inputs and fitting the network so that the representation is consistent with the measurements. Using a Fourier-feature MLP is critical for our approach since it enables us to impose a strong spatial and temporal prior on the heart to be reconstructed. Our contributions are as follows:

- We propose an approach for cardiac real-time MRI based on parameterizing the beating heart with an MLP with Fourier-feature inputs. The method allows controlling the spatial and temporal regularization strength through the setup of the Fourier-feature inputs.
- We compare our approach to the time-dependent deep image prior (t-DIP) [Yoo+21], a state-of-the-art untrained method based on CNNs. We study the reconstruction quality and computational cost on various datasets in different operating regimes, including different image resolutions, slice thicknesses, and acquisition lengths, and find our method performs on par in terms of image quality, sometimes even marginally better, but at a higher computational cost.
- Compared to two very recently proposed approaches [Hua+22; Fen+23] also based on implicit neural representations, we achieve better image quality at a higher computational cost.

Specifically, Huang et al. [Hua+22] enable cardiac MRI by fitting a Fourier-feature MLP directly to the measurements in the Fourier domain. Fitting the MLP in the Fourier domain has the advantage of being faster compared to fitting it in the image domain. However, this comes at a significant loss in image quality, as we show later, since Fourier-feature MLPs are not a good model for representing an image in the Fourier domain. Specifically, an image is relatively smooth, whereas the spectrum of an image is not smooth, and a Fourier-feature MLP has a bias towards fitting smooth signals.

Feng et al. [Fen+23]’s method is based on fitting an MLP with hash encoding to the data. Using a hash encoding also has computational benefits over our approach, but a hash encoding is not an effective image prior, thus the method requires additional explicit regularization.

2 Related Work

In this section, we briefly discuss classical approaches to cardiac real-time MRI, implicit neural networks and CNN-based neural networks for medical image reconstruction.

Approaches to cardiac MRI with sparse and low-rank regularization techniques A variety of classical approaches to cardiac MRI are based on regularization in the spatial and temporal dimensions with hand-crafted signal priors. For example, Feng et al. [Fen+14] impose a total-variation norm penalty over time and Feng et al. [Fen+16] impose a total-variation penalty over cardiac phases.

Another line of work incorporates temporal relations by assuming low-rank structures within the temporal series of images, through low-rank tensor decompositions [Chr+18], through decompositions into image patches of low-rank [Jia+18], and through multi-scale low-rank decompositions [Ong+20].

Besides these linear signal models, methods have been developed that assume low-rankness in a kernel space [Nak+17; Pod+19] or assume that the images lie on a smooth low-dimensional manifold [PJ16; Ahm+20].

Implicit neural networks Our work relies on representing time-varying signals with an implicit neural network, i.e., a function parameterized by a neural network that maps a spatial coordinate vector and a time variable to a pixel value. Implicit neural networks are successfully used for representing images and volumes in a variety of applications. The architecture of the network is important, for images and volumes transforming the coordinates with a Fourier-feature map before passing them through a multi-layer perceptron works well, and most current architectures including NeRF [Mil+20], SIREN [Sit+20], and MLPs with Fourier-feature inputs [Tan+20] use this architecture.

Implicit networks for medical imaging Implicit neural networks are excellent image models and can therefore be used as an image prior for image reconstruction tasks, as demonstrated by Tancik et al. [Tan+20] on a toy dataset. Subsequently, Shen et al. [SPX22] have improved the reconstruction quality for static CT and MRI imaging by pre-training the network on a previously reconstructed image of the same subject. Shen et al. [SPX22] also reconstructed a temporal series of 3D images, and used the first image for pre-training the network. Contrary to our approach, the method does not model temporal variations.

Implicit networks have also been used for super-resolution tasks in medical imaging, for example for obtaining high-resolution 3D MRI [Wu+21] from low-resolution 2D images, and for building a scale-agnostic model for MRI [VV+22].

Implicit networks for dynamic MRI reconstruction As mentioned before, most related to our work are two recent methods using implicit networks for dynamic MRI reconstruction. Huang et al. [Hua+22] introduced the method NIK which uses a SIREN network [Sit+20] with additional explicit regularization to represent the signal in k-space. It outputs a k-space value given the k-space coordinate, the time, and the measurement coil index. Once the network has been trained on the measured frequencies, it can be evaluated at the missing k-space frequencies to yield a reconstructed k-space. We compare our approach to a variant of NIK called k-space Fourier-feature MLP (KFMLP) that we introduce in the methodology section.

Feng et al. [Fen+23] learn a neural representation of the dynamic object in the image domain. The implicit network is implemented by an MLP with a hash-encoding for the input coordinates. The MLP is small in size compared to our methods and can be evaluated very efficiently. However, the method relies on additional explicit regularization of the images’ temporal total variation and an additional loss term to enforce low-rankness of the solution. Thus, the method relies on explicit regularization and not on an implicit bias inherent to the network architecture as we do.

Untrained methods based on CNNs Our approach relies on regularization with a neural network in the form of an MLP with Fourier-feature inputs. We find that the network has a regularizing effect that is very similar to state-of-the-art untrained CNNs.

Untrained neural networks enable image reconstruction by fitting a neural network to the measurement data, as observed by Ulyanov et al. in the seminal DIP paper [UVL20]. Very simple CNNs enable excellent signal reconstruction performance without any training since CNNs can be excellent image priors [HH19], and provably reconstruct smooth signals [HS20b; HS20a]. Untrained networks can outperform classical sparsity based reconstruction for accelerated MRI [DH21].

The method time-dependent deep image prior (t-DIP) [Yoo+21] extends the deep image prior [UVL20] to dynamic MRI. Like our approach, the t-DIP fits a single model to the entire series of images, and time is used as an input coordinate. In contrast to using a CNN to regularize in the spatial dimension, we model both the temporal and the spatial dimensions through an implicit network.

The method Gen-SToRM [Zou+21] trains a CNN to generate a temporal series of images from a temporal series of low-dimensional network inputs. The network inputs are trained jointly with the CNN. The temporal derivative of the network inputs and the CNNs Jacobian are regularized to favour reconstructions that are on a smooth low-dimensional manifold in image space and that vary smoothly in time. A conceptually similar method has been applied for video reconstruction [HA20] aside from the context of MRI reconstruction.

3 Problem Formulation

Our goal is to reconstruct a video of a moving object from sequentially acquired under-sampled linear measurements. We consider an object $\mathbf{x}(\sigma) \in \mathbb{R}^{w \times h}$ in the form of an image with width w and height h that is parameterized by a motion state σ . In our setup, the object $\mathbf{x}(\sigma)$ is the image of a heart at a certain state in the cardiac and respiratory cycle.

We consider the standard MRI measurement model, where we collect noisy linear measurements

$$\mathbf{y}_{\tau,c} = \mathbf{M}_{\tau} \mathbf{F} \mathbf{S}_c \mathbf{x}(\sigma_{\tau}) + \mathbf{n}_{\tau,c} \quad (1)$$

at the receiver coils $c = 1, \dots, C$. Here, \mathbf{F} is the 2-D Fourier matrix, \mathbf{S}_c is a diagonal matrix containing the sensitivities of receiver coil c , and \mathbf{M}_{τ} is a binary sampling mask encoding the frequencies collected during time τ . In this work, we consider Cartesian sampling patterns. The measurements are distorted by additive noise $\mathbf{n}_{\tau,c}$.

Note that the object $\mathbf{x}(\sigma)$ is changing continuously. The measurement model (1) assumes that the object is essentially constant during a very short time frame which we index by τ . During this short time frame, only very few measurements (frequencies as selected by the mask \mathbf{M}_{τ}) are collected.

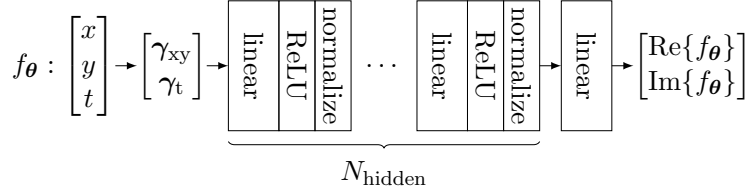


Figure 1: The FMLPs’ network consists of separate spatial and temporal Fourier-feature embeddings that are concatenated, followed by an MLP that outputs the complex image intensity at the specified coordinate.

The measurements from different coils can be stacked into a single measurement vector

$$\mathbf{y}_\tau = \mathbf{A}_\tau \mathbf{x}(\sigma_\tau) + \mathbf{n}_\tau,$$

where $\mathbf{y}_\tau = [\mathbf{y}_{\tau,1}^T, \dots, \mathbf{y}_{\tau,C}^T]^T$ and $\mathbf{n}_\tau = [\mathbf{n}_{\tau,1}^T, \dots, \mathbf{n}_{\tau,C}^T]^T$. The matrix \mathbf{A}_τ is the resulting forward map for frame τ .

Our goal is to reconstruct the image series (or video) $\mathbf{x}(\sigma_\tau)$, $\tau = 1, \dots, T$ from the noisy measurements \mathbf{y}_τ . During each time frame indexed by τ , only very few measurements are collected. Therefore, reconstructing each frame individually results in poor image quality, even if we take prior information about the image into account. Successful reconstruction relies on using prior information about the images in spatial directions as well as in the temporal direction.

Note that in our problem formulation, the index τ refers to a short time frame that is used for binning the measurement data such that motion can be neglected. This time frame may not necessarily correspond to the time frame that is used in the video that is ultimately rendered. Thus, the generation of the final video might require re-sampling at a different frame rate. An advantage of our method based on implicit representation is that we can use different frame rates for reconstruction and for the output showed to the end-user.

4 Methods

Our FMLP method is based on parameterizing the object $\mathbf{x}(\sigma)$ with a Fourier-feature MLP and fitting the neural network to the measurement data. Once fitted, we query the neural network to generate a video as an output. The Fourier-feature MLP we use is a good prior for a (slowly) time-varying smooth object, and we use no other regularization for reconstruction.

We parameterize the object $\mathbf{x}(\sigma)$ by a neural network $f_\theta : \mathbb{R}^3 \rightarrow \mathbb{R}^2$ mapping a spatio-temporal coordinate vector $\mathbf{c} = [x, y, t]^T$ to a complex image intensity value, represented by a real and an imaginary part. We focus on 2D images, but the method can easily be extended to 3D by adding another spatial coordinate so that $\mathbf{c} = [x, y, z, t]$. The coordinates x and y denote physical locations within the field of view measured in meters, and the time-coordinate t is time measured in seconds. The origins of the spatial and temporal coordinate axes can be set arbitrarily as the particular neural network that we use is shift-invariant. We define $t = 0$ s as the beginning of the measurement process. For computing a pixel-based image $f_\theta(t_\tau)$ at time t_τ , the network f_θ is evaluated on a regular grid of spatial coordinates within the field of view with the temporal coordinate fixed to t_τ .

We fit a network by minimizing the reconstruction loss defined as

$$\mathcal{L}(\boldsymbol{\theta}) = \frac{1}{T} \sum_{\tau=1}^T \|\mathbf{A}_\tau \mathbf{f}_\theta(t_\tau) - \mathbf{y}_\tau\|_2^2.$$

The time t_τ is chosen to be at the center of the acquisition time window of frame τ and the spatial coordinate grid used for computing $\mathbf{f}_\theta(t_\tau)$ is matched to the Cartesian sampling grid in k-space. After fitting, reconstructed images can be sampled from the implicit representation as $\hat{\mathbf{x}}(\sigma_\tau) = \mathbf{f}_\theta(t_\tau)$.

The network architecture is critical for performance. Our architecture is based on using Fourier-features as inputs to a ReLU-MLP and is depicted in Figure 1. The Fourier-feature inputs are used in a variety of implicit neural network architectures [Tan+20; Sit+20; Mil+22]. The Fourier-feature layer embeds the spatial coordinates and the temporal coordinate separately as $\boldsymbol{\gamma}(\mathbf{c}) = [\boldsymbol{\gamma}_{\text{spatial}}([x, y]), \boldsymbol{\gamma}_{\text{temporal}}(t)]^T$ with

$$\begin{aligned} \boldsymbol{\gamma}_{\text{spatial}}([x, y]) &= \left[\sin \left(\mathbf{B} \begin{bmatrix} s_x x \\ s_y y \end{bmatrix} \right), \cos \left(\mathbf{B} \begin{bmatrix} s_x x \\ s_y y \end{bmatrix} \right) \right]^T, \\ \boldsymbol{\gamma}_{\text{temporal}}(t) &= [\sin(\mathbf{b} s_t t), \cos(\mathbf{b} s_t t)]^T. \end{aligned}$$

Here, the sin and cos functions are applied element-wise. The coordinates are scaled by hyperparameters s_x , s_y , and s_t with units $\frac{1}{\text{m}}$ and $\frac{1}{\text{s}}$, respectively, which control the variance of the angular frequencies in the spatial and temporal dimensions. The elements in the matrix \mathbf{B} and the vector \mathbf{b} are drawn independently from a zero-mean Gaussian distribution with unit variance $\mathcal{N}(0, 1)$ and are fixed and not optimized over. We choose $\mathbf{B} \in \mathbb{R}^{256 \times 2}$ and $\mathbf{b} \in \mathbb{R}^{64}$ for a total feature size of $512 + 128$.

We observed that embedding the spatial and temporal coordinates separately leads to sharper reconstructions compared to the intuitive setup of having one Fourier-feature embedding for all three coordinates together, see Section A.4 in the supplementary material.

The MLP takes the Fourier-feature vector $\boldsymbol{\gamma}(\mathbf{c})$ as input. After each linear hidden layer, the ReLU activation is applied and the output feature vector is normalized to zero mean and unit variance. The output layer has two neurons with a linear activation function and without normalization, which output the real and imaginary part of the complex image intensity value, respectively. The weights of the linear layers are initialized by drawing from $\mathcal{N}(0, \sigma_{\text{linear}}^2)$, where the variance σ_{linear}^2 can be tuned. The final output is multiplied by a constant s_{out} that is tuned as a hyperparameter depending on the scaling of the k-space data and the sensitivity maps. In our implementation, we set $\sigma_{\text{linear}} = 0.01$ and the MLP consists of 7 hidden layers with 512 neurons each if not explicitly stated otherwise.

4.1 Baseline methods

In our experimental results, we consider two methods described in more detail below for comparison. The first method is a variant of Huang et al. [Hua+22]’s NIK method that is based on fitting a Fourier-feature MLP in the Fourier domain. We consider a variant of the method and not the original one, since code for the original is not available, our sampling setup is different, and we wanted to get best performance when using a Fourier-feature MLP in the Fourier domain, which

required us to deviate from NIK. The second method we compare to is the time-dependent DIP [Yoo+21], a state-of-the-art untrained method based on CNNs.

4.1.1 Fourier-feature MLP as implicit k-space prior (KFMLP)

The KFMLP is conceptually similar to the NIK [Hua+22] that has been proposed recently. It parameterizes the time-varying k-space $\mathbf{F}\mathbf{S}\mathbf{x}(\sigma)$ with a neural network. The network $f_{\theta} : \mathbb{R}^3 \rightarrow \mathbb{R}^{2C}$ maps frequency-time coordinates $[k_x, k_y, t]$ to complex k-space values that are represented by a real and an imaginary part for each of the C receiver coils. The frequency-coordinates k_x and k_y are normalized to $[-\pi, \pi)$ and the time-coordinate t , as for the FMLP, measures time in seconds. The network is fitted to the measured k-space data at frequency-time coordinates along the sampling trajectory. For computational purposes, we segment the trajectory into frames that are treated as samples of the dataset. Specifically, we evaluate the network f_{θ} at the k-space coordinates and sampling times that correspond to the measurements in the vectors \mathbf{y}_{τ} . The resulting reconstructed k-space along the trajectory of frame τ is denoted as $\mathbf{f}_{\theta, \tau}^{\text{traj}}$. We minimize a similar loss as proposed for the NIK [Hua+22],

$$\mathcal{L}(\theta) = \frac{1}{T} \sum_{\tau=1}^T \mathcal{L}_{\text{HDR}}(\mathbf{f}_{\theta, \tau}^{\text{traj}}, \mathbf{y}_{\tau}) + R(\mathbf{f}_{\theta, \tau}^{\text{traj}}).$$

The loss is composed by a high dynamic range reconstruction loss and an explicit k-space regularization term. The high dynamic range loss is defined as

$$\mathcal{L}_{\text{HDR}}(\hat{\mathbf{y}}_{\tau}, \mathbf{y}_{\tau}) = \left\| \frac{\hat{\mathbf{y}}_{\tau} - \mathbf{y}_{\tau}}{|\text{sg}(\hat{\mathbf{y}}_{\tau})| + \varepsilon} \right\|_2^2.$$

Here, the operator $\text{sg}(\cdot)$ stops the propagation of the gradient during back-propagation, $|\cdot|$ computes the absolute value accounting for the positive and negative k-space values, and $\varepsilon > 0$ is a hyperparameter that adjusts the compression of the dynamic range. The division is computed element-wise. Note that our definition of the high dynamic range loss differs from the NIK that does not take the absolute value in the denominator.

The k-space regularization term $R(\mathbf{f}_{\theta, \tau}^{\text{traj}})$ is adopted from the NIK and is defined as

$$R(\mathbf{f}_{\theta, \tau}^{\text{traj}}) = \lambda_{\text{denoiser}} \mathcal{L}_{\text{HDR}}(\mathbf{f}_{\theta, \tau}^{\text{traj}}, \mathbf{K}_{\tau} \mathbf{f}_{\theta, \tau}^{\text{traj}}),$$

where \mathbf{K}_{τ} is a diagonal matrix with entries $e^{-d/2\sigma^2}$ that weight the k-space values according to their respective coordinate distances $d = \sqrt{k_x^2 + k_y^2}$ to the k-space center. The hyper-parameters $\lambda_{\text{denoiser}} > 0$ and $\sigma > 0$ adjust the regularization strength. By ablation studies, we find that $\varepsilon = 10^4$, $\sigma = 10$ and $\lambda_{\text{denoiser}} = 0.1$ yield good results for our datasets. Note that the high dynamic range reconstruction loss and the k-space regularization term are not essential, but they yield a small improvement compared to using the standard l_2 reconstruction loss without any explicit k-space regularization, see Section B.2 and Section B.3 in the supplementary materials.

After training, a reconstructed image of at time t_{τ} is obtained by evaluating the network at all frequencies on the Cartesian grid and combining the reconstructed k-spaces via coil combination. The reconstructed k-space on the Cartesian grid, with time coordinate fixed to t_{τ} , is denoted

by $\mathbf{f}_{\boldsymbol{\theta}}^{\text{grid}}(t_{\tau})$ that stacks the reconstructed k-spaces $\mathbf{f}_{\boldsymbol{\theta},c}^{\text{grid}}(t_{\tau})$ of the receiver coils $c = 1, \dots, C$. A coil-combined image is computed as

$$\hat{\mathbf{x}}(\sigma_{\tau}) = \sum_{c=1}^C \bar{\mathbf{S}}_c^* \mathbf{F}^{-1} \mathbf{f}_{\boldsymbol{\theta},c}^{\text{grid}}(t_{\tau}),$$

where $\bar{\mathbf{S}}_c^*$ denotes the complex conjugate of the normalized sensitivity map of coil c given as

$$\bar{\mathbf{S}}_c = \left(\sum_{j=1}^C \mathbf{S}_j^* \mathbf{S}_j \right)^{-1} \mathbf{S}_c.$$

The KFMLP uses the same network architecture as the FMLP with Fourier-features that are given as input to an MLP with ReLU activation function and normalization. The k-space coordinates are embedded in a separate Fourier-feature vector from the time coordinate. Again, the coordinate scales s_x , s_y , and s_t are tuned as hyper-parameters.

The KFMLP architecture differs slightly from the NIK architecture that uses a sinusoidal activation function, jointly embeds the time and k-space coordinates, and treats the coils $c = 1, \dots, C$ as an additional input dimension.

4.1.2 Time-dependent DIP

We implement the time-dependent DIP [Yoo+21] which is a state-of-the-art method for untrained reconstruction. It uses a CNN with time-varying network inputs as implicit prior. The time-varying network inputs are generated by embedding a temporal input coordinate on a helix trajectory and then mapping the embedding to the CNN’s input features using a small fully connected network.

The helix is a trajectory in \mathbb{R}^3 with unit radius and slope z_{slack} that we tune as a hyperparameter. The angular frequency of the helix introduces prior information about the heart rate and periodicity of motion. For matching the angular frequency of the helix with the heart rate, an estimate of the number of cardiac cycles is required, which we obtain from an electrocardiogram (ECG).

Due to the validation lines that are extracted at random positions, the frames are not equally spaced in time. We account for the deviation by modifying the sampled positions on the helix trajectory. Instead of sampling equally spaced points based on the frame index k as proposed by the authors, we use the measurement time t_{τ} to ensure that the extraction of validation lines does not diminish the performance of the t-DIP. The sampled positions on the helix are mapped to a more expressive latent space by a small MLP called MapNet. The output of the MapNet is reshaped as input for the subsequent CNN.

We adopt the CNN architecture but modify it to fit our image resolution. The proposed architecture of the CNN up-samples the feature resolution in powers of two using nearest-neighbor interpolation. We adjust the input feature resolution and the number of up-sampling layers to obtain an output resolution that is close to our target resolution. The output image is then center-cropped to the target resolution. Between interpolation layers, two convolutional layers are applied. We tune the channel depth of the convolutional layers as a hyperparameter.

5 Experiments and Results

We assess the reconstruction quality and computational demands of FMLP on real data that we collected as well as on phantom data in the supplementary material. We compare to the KFMLP method and the time-dependent DIP, and find that FMLP performs as well as the t-DIP and significantly better than KFMLP in terms of image quality, but at a higher computational cost than both methods. Code to reproduce the results is available at <https://github.com/MLI-lab/cinemri>.

5.1 Datasets

We conduct experiments on datasets that were acquired on a 3T Elition X scanner (Philips Healthcare, The Netherlands). The scans are taken of a healthy 30 years old male volunteer. This study was approved by the local ethics committee and written informed consent was obtained.

Measurement data was acquired at two different resolutions $2.27 \times 2.26 \text{ mm}^2$ (264×186 acquisition matrix size) and $1.25 \times 1.26 \text{ mm}^2$ (480×334), with 10 mm and 5 mm slice thickness, respectively. We refer to those as 'low-resolution high-SNR' and 'high-resolution' datasets. A third dataset was acquired at low resolution with a reduced (isotropic) slice thickness of 2.25 mm, decreasing the signal strength and the signal-to-noise ratio (SNR). This dataset is referred to as the 'low-resolution low-SNR' dataset. For each of those configurations, a breath-hold triggered scan and a free-breathing scan were taken. The acquisition length was set retrospectively for the free-breathing scan and we conduct experiments with 4.0s, 8.0s, and 15.9s of acquired data.

For the breath-hold scan, the data acquisition is triggered by an ECG such that measurements of similar cardiac phases are binned. The dynamics are then reconstructed with a sparsity-based reconstruction method for static MRI which the MRI scanner performs by default. The breath-hold reconstructions serve as a visual reference for the free-breathing reconstructions.

During the free-breathing scan, measurements are acquired continuously (ungated). We use a partial-Fourier Cartesian sampling pattern, where the k-space is fully sampled along the k_x -dimension (frequency-encoding) and randomly under-sampled along the k_y -dimension (phase-encoding). Thus, measurements are taken sequentially along k_y -lines in the k-space. The measured k_y -lines are binned into frames retrospectively. Further details on the measurement parameters are listed in Section E in the supplementary materials.

5.2 Performance metrics and quality criteria

It is common practice to measure the image quality of reconstruction methods with full-reference image quality metrics, such as the structural similarity index measure (SSIM) [Wan+04] or the visual information fidelity (VIF) [SB06]. For our synthetically generated phantom dataset in the supplement (see Section C), we measure performance with those metrics.

For our original data (and original data in the context of real-time MRI in general), ground-truth images are not available. We therefore measure performance in terms of an estimate of the MSE as well as through visual comparisons.

Specifically, we visually compare the reconstructed images to the ECG-triggered breath-hold reconstructions obtained from the scanner by binning-based reconstruction methods using sparsity regularization. We focus on anatomic details with the region of interest, the heart, such as papillary muscles in the left ventricle that are rapidly changing shape during systoles.

We estimate a normalized version of the mean squared error based on a hold-out set of randomly subsampled frequencies as follows. We randomly extract 5 % of the measured k_y -lines for validation. The remaining k_y -lines are binned into frames $\tau = 1, \dots, T$ for training, such that the k-space of every frame contains $N_{\text{lines}} = 6$ many k_y -lines. Each validation line $\mathbf{y}_v, v = 1, \dots, V$ is assigned to the frame τ_v that is closest in sample time. Let $\hat{\mathbf{y}}_v$ be the reconstructed k-space lines predicted by a reconstruction algorithm (FMLP, KFMLP, and t-DIP in our setup). The lines are obtained by first applying the sensitivity maps and Fourier transform to the reconstructed images $\hat{\mathbf{x}}(\sigma_{\tau_v})$ and then extracting the k_y -line corresponding to \mathbf{y}_v . We estimate the signal-to-error ratio (SER) as a metric for quantifying data consistency

$$\text{SER} = 10 \log_{10} \frac{\sum_{v=1}^V \|\mathbf{y}_v\|_2^2}{\sum_{v=1}^V \|\hat{\mathbf{y}}_v - \mathbf{y}_v\|_2^2}.$$

5.3 Implementation details

We implemented the FMLP, KFMLP, and t-DIP using PyTorch. The models are optimized using Adam [KB17] with learning rate 2×10^{-4} for the FMLP and the KFMLP, and learning rate 1×10^{-4} for the t-DIP. The models are trained until no new SER high-score has been reached for 200 epochs. We evaluate the reconstruction quality at the epoch of maximum SER. The experiments are conducted on a server equipped with a RTX 6000 GPU with 24 GB VRAM and an Intel(R) Core(TM) i9-9940X CPU with 128 GB available RAM.

5.4 Quantitative reconstruction quality analysis

In this section, we quantitatively compare the reconstruction quality of the FMLP, the KFMLP, and the t-DIP in terms of the estimated normalized MSE (specifically, in terms of the SER defined in the previous section).

Different operating regimes We start by comparing the image reconstruction quality measured in terms of the SER in different operating regimes that feature different image resolutions and slice thicknesses. Specifically, we fit all three methods to the low-resolution high-SNR dataset, the low-resolution low-SNR dataset, and the high-resolution dataset. The hyper-parameters of the models are tuned on each dataset individually and the methods are trained on $T = 225$ frames.

The results in Table 1 show that the FMLP and the t-DIP achieve a similar SER with marginal differences in all evaluated operating regimes. While the t-DIP achieves a slightly higher SER than the FMLP on the low-resolution high-SNR dataset, the FMLP performs slightly better on the low-resolution low-SNR and the high-resolution datasets. The KFMLP, learning a representation of the k-space, achieves much lower SER scores than the FMLP or the t-DIP. The difference is substantial on all evaluated datasets.

Performance as a function of acquisition length Next, we study the reconstruction quality for different measurement acquisition length. We measure the image quality in terms of the SER within the first 4 s of reconstructed images, while training the methods on increasing acquisition

dataset	FMLP	KFMLP	t-DIP
low-resolution, high-SNR	17.16	12.53	17.19
low-resolution, low-SNR	10.62	8.64	10.59
high-resolution	9.00	6.51	8.97

Table 1: Maximum SER of the models on datasets in different operating regimes. FMLP and t-DIP perform similarly, while KFMLP performs significantly worse.

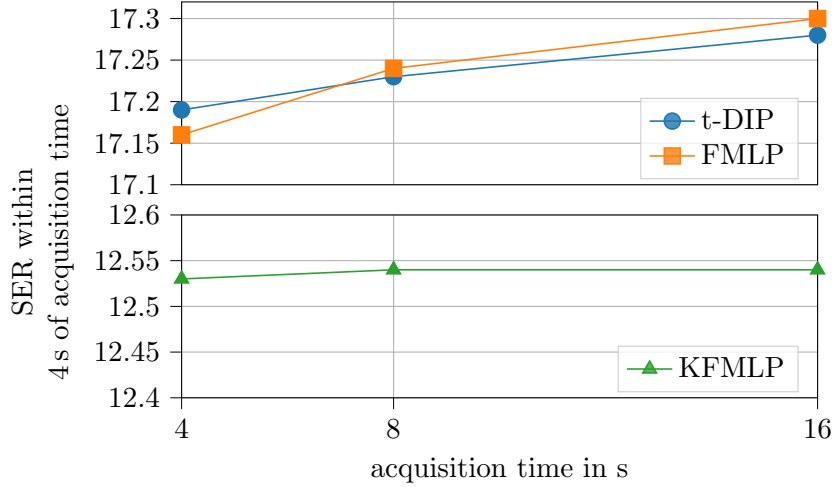


Figure 2: The validation SER within the first 4s of acquisition time improves with increasing the amount of measurement data beyond 4s. The reconstruction quality can be improved by training the model on a longer acquisition time. The models were trained on the low-resolution high-SNR dataset with the same configurations as in Figure 3 and $z_{\text{slack}} = 0.1, 0.2$, and 0.4 for $T = 225$ (4s), 450 (8s), and 900 (16s), respectively.

lengths, i.e., on 4s, 8s, and 16s of acquired data, respectively. The experiment is conducted on the low-resolution high-SNR dataset.

Figure 2 shows that the SER of the FMLP and the t-DIP improves when training the methods on more data, indicating that both methods not only take advantage of temporal correlations between adjacent frames but also over the entire acquisition length. The KFMLP, by contrast, does not improve substantially. Remarkably, the FMLP and the t-DIP improve by a similar margin even though the t-DIP uses prior information about the heart rate that is encoded by the angular frequency of the helix trajectory. Information about the cardiac phase might be advantageous for correlating frames over multiple cardiac cycles. The FMLP does not incorporate such prior but nevertheless improves at a similar rate as a function of the acquisition length.

5.5 Visual quality assessment

We compare the reconstructed images of the FMLP, the KFMLP, and the t-DIP to the ECG-triggered breath-hold reconstructions that serve as a visual reference. The methods are compared on the low-resolution high-SNR, the low-resolution low-SNR, and the high-resolution dataset. For each

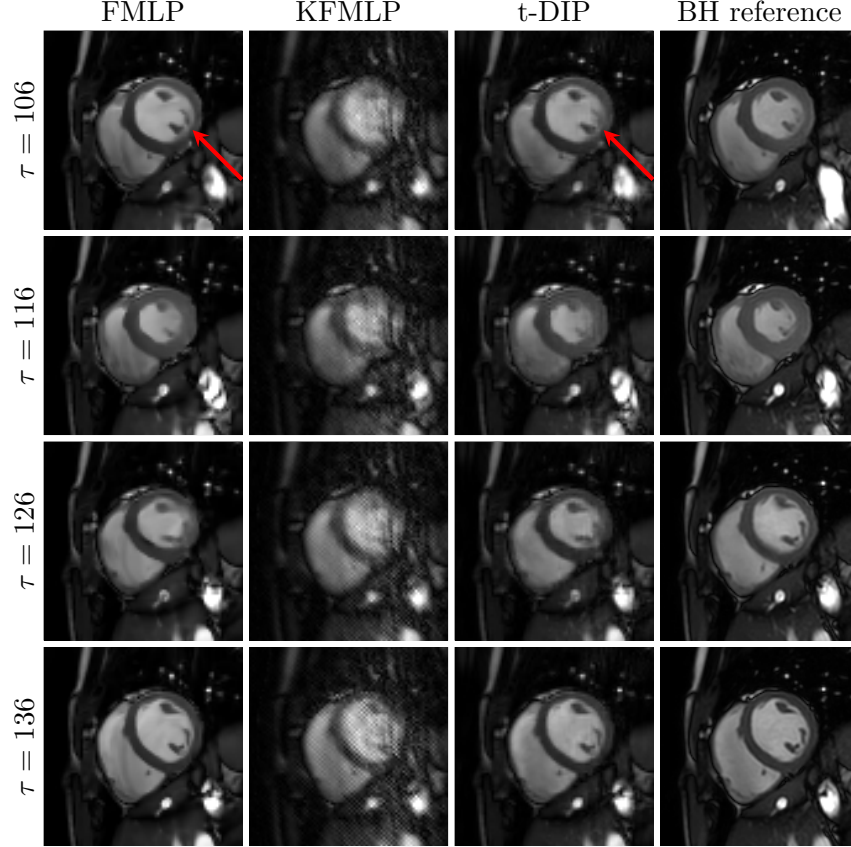


Figure 3: On the low-resolution high-SNR dataset, the image quality of the FMLP and the t-DIP are similar, whereby the FMLP recovers anatomic details such as the papillary muscles in the left ventricle (red arrow) more accurately. The reconstructions by the KFMLP are distorted by aliasing-like artifacts and fine-structured noise such that anatomic details are well not recognizable. The models were trained on $T = 225$ frames. The hyperparameter configuration are $s_x = s_y = 30 \text{ m}^{-1}$, $s_t = 1 \text{ s}^{-1}$, 7 hidden layers, 512 neurons per hidden layer for the FMLP, $s_x = s_y = 15$, $s_t = 1 \text{ s}^{-1}$, 7 hidden layers, 512 neurons per hidden layer for the KFMLP, and 256 channels and $z_{\text{slack}} = 0.1$ for the t-DIP.

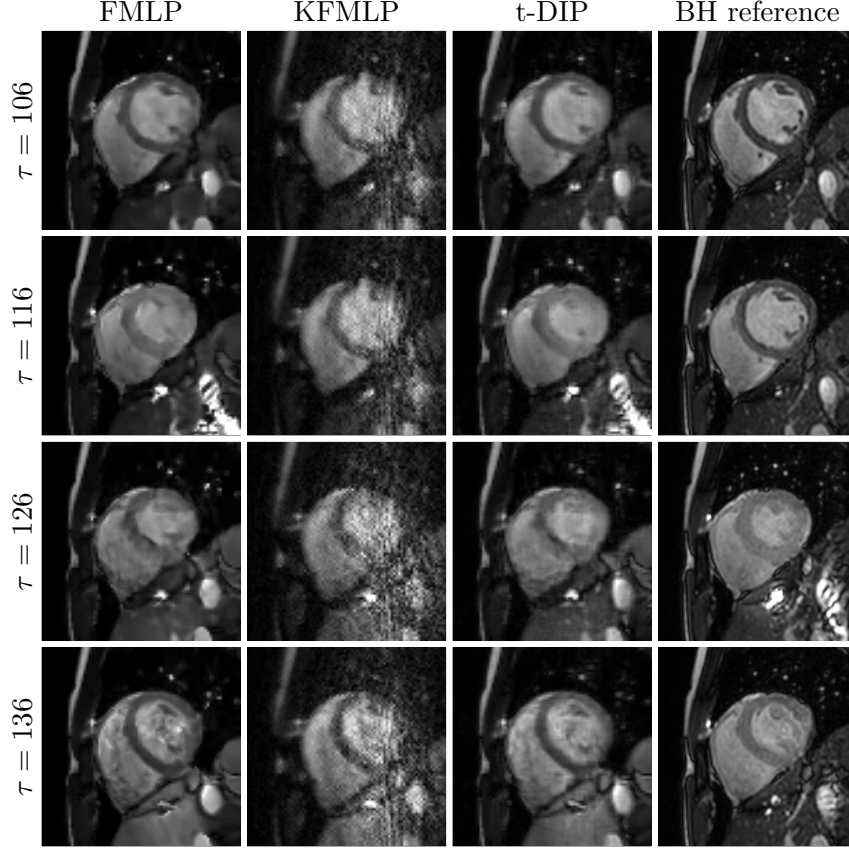


Figure 4: For an isotropic slice thickness (low-resolution low-SNR dataset) the reconstruction quality of all methods degrades and new artifacts are introduced. The FMLP and the t-DIP achieve a similar image quality and outperform the KFMLP. The models were trained on $T = 225$ frames. The hyperparameter configuration are: $s_x = s_y = 30 \text{ m}^{-1}$, $s_t = 2 \text{ s}^{-1}$, 5 hidden layers, and 256 neurons per hidden layer for the FMLP, $s_x = s_y = 15$, $s_t = 1 \text{ s}^{-1}$, 7 hidden layers, and 512 neurons per hidden layer for the KFMLP, and 256 channels and $z_{\text{slack}} = 0.5$ for the t-DIP.

dataset, we show reconstructions of four frames that have been selected to cover a cardiac cycle.

The reconstructions in the Figures 3, 4, and 5, show that FMLP performs on par with the t-DIP in terms of perceived image quality. Although the overall differences in quality are marginal, the FMLP recovers anatomic details slightly more accurately on the low-resolution high-SNR dataset. The differences are most apparent in small moving anatomic structures of the heart, such as the papillary muscles, see Figure 3. On the low-resolution low-SNR and the high-resolution datasets, the FMLP and the t-DIP exhibit similar artifacts, see Figures 4, and 5.

We find that the FMLP achieves a better image quality compared to the KFMLP on all datasets. On the low-resolution high-SNR dataset, the KFMLP suffers aliasing-like artifacts that blur anatomic details, such as the papillary muscles, see Figure 3. On the low-resolution low-SNR dataset, the aliasing-like artifacts are superimposed by the noise that further degrades the image quality compared to the FMLP (Figure 4). However, the noise of the KFMLP becomes most prominent on the high-resolution dataset, where it obscures any meaningful details in the cardiac

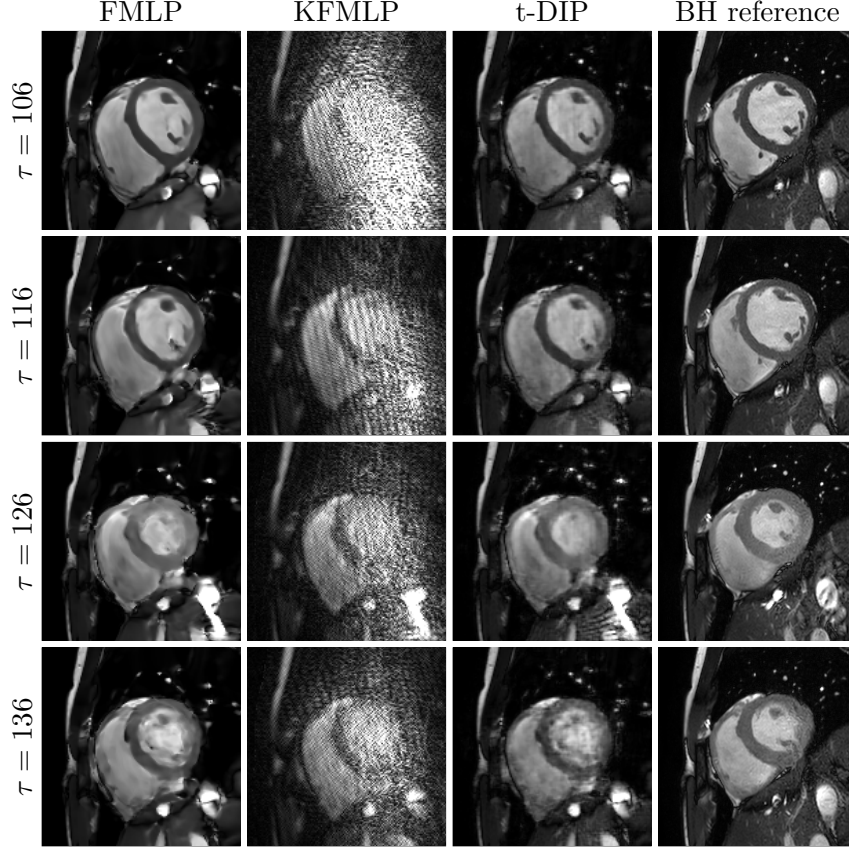


Figure 5: On the high-resolution dataset, the FMLP and the t-DIP achieve a similar reconstruction quality and both methods suffer from similar artifacts. The quality of the KFMLP is decreased substantially by noise-like artifacts. The models were trained on $T = 225$ frames. The hyperparameter configuration are: $s_x = s_y = 30 \text{ m}^{-1}$, $s_t = 1.0 \text{ s}^{-1}$, 7 hidden layers, 512 neurons per hidden layer for the FMLP, $s_x = s_y = 10$, $s_t = 1.0 \text{ s}^{-1}$, 7 hidden layers, 512 neurons per hidden layer for the KFMLP, and 256 channels and $z_{\text{slack}} = 0.5$ for the t-DIP.

region (Figure 5).

5.6 Computational cost

The exact computational costs depend on the hyperparameter configuration, but for most of our tested hyperparameter configurations, training the FMLP requires more epochs and takes longer to train per epoch than the t-DIP and the KFMLP. The KFMLP and the t-DIP reach the maximum SER in a similar amount of training time, whereas the t-DIP converges in fewer epochs.

The computational performance characteristics of the configurations with the highest SER are listed in Table 2. We report the model sizes, memory requirements during training, training time per epoch, and training time until the maximum SER is reached on the low-resolution high-SNR dataset and on the high-resolution dataset, each with $T = 225$ frames. The total training time is measured by the wall-clock time and includes data-loading, computation of the SER for validation, and logging the training progress. The time per epoch is measured by the wall-clock time over 100 epochs of

res.	property	FMLP	KFMLP	t-DIP
186×264	# parameters	1.91×10^6	1.93×10^6	5.94×10^6
	memory on GPU	3.55 GB	1.14 GB	1.94 GB
	time per epoch	19.92 s	4.06 s	8.56 s
	number of epochs	744	309	252
	total training time	510 min	35 min	42 min
334×480	# parameters	1.91×10^6	1.93×10^6	7.12×10^6
	memory on GPU	9.21 GB	1.22 GB	4.03 GB
	time per epoch	63.82 s	4.11 s	26.65 s
	number of epochs	1872	601	176
	total training time	3237 min	110 min	91 min

Table 2: Computational performance characteristics.

training without additional overhead. The hyperparameter configurations with maximum SER are chosen that are specified in Figure 3 and 5. Note that the t-DIP’s CNN uses five up-sampling layers on the low-resolution dataset, whereas six up-sampling layers are required on the high-resolution dataset.

We note that the computational demands required for training scale differently with image resolution for the three methods. An advantage of the FMLP is that the network size can stay constant as the image resolution is increased. However, the network has to be evaluated for all pixels and, thus, the computational demands scale linearly with image resolution. The CNN of the t-DIP, by contrast, needs to be adapted to an increasing image resolution by adding up-sampling layers and convolutional layers. Thus, the number of trainable parameters increases with image resolution. However, doubling the image resolution merely requires adding one more stage of up-sampling and convolutional layers. Thus, the cost of evaluating the CNN scales efficiently with image resolution. The network size of the KFMLP can also be set independently of the image resolution. Moreover, the computational demands do not scale with the image resolution but with the number of measured coordinates. The network is evaluated on the full Cartesian grid only once after training.

6 Discussion and Conclusion

We proposed an untrained reconstruction method based on implicit networks, called FMLP, for cardiac real-time MRI. The method uses an ReLU-MLP with Fourier-feature inputs to encode spatio-temporal coordinate vectors for representing an image of the beating heart. We evaluated the method on experimental datasets for 2D free-breathing cardiac real-time MRI covering different operating regimes, i.e., different image resolutions, slice thicknesses, and acquisition lengths.

We find that FMLP can achieve reconstruction quality on par or slightly better with the best CNN-based untrained methods (t-DIP), as measured with quantitative metrics (SER) and as determined through visual comparisons. FMLP tends to improve slightly faster as a function of the acquisition time (see Figure 2), and slightly surpassed t-DIP for longer acquisition times. The FMLP only relies on the implicit neural network for regularization.

We note that the similarity in performance to the t-DIP is somewhat expected since MLPs with Fourier-feature inputs and CNNs both have a bias towards fitting smooth images and low-frequency

contents of the signal first [Tan+20; HS20b]. This implicit bias suppresses high-frequency aliasing artifacts, thereby interpolating the missing frequencies in the k-space and reconstructing the image.

While an MLP with Fourier-features is a good image model, it is not a good model for representing an image in the Fourier domain. We found that KFMLP, which relies on representing the signal in the Fourier domain with a Fourier-feature MLP, suffered from aliasing and noise-like artifacts that distorted the images considerably. Although the KFMLP learned to represent the measurements along the sampling trajectory well, it poorly generalized to frequencies that had not been measured. We note that the partial-Fourier random Cartesian sampling pattern used for the experiments may pose an especially difficult challenge to the reconstruction methods as a small subset of k-space lines is measured repetitively. Thus, a large fraction of the k-space is not measured at any time and needs to be interpolated with an efficient image model. Huang et al. [Hua+22] tested the NIK (the KFMLP is a variant of the NIK) on retrospective data with a golden-angle radial trajectory. On such data, the method did not suffer from strong artifacts compared to the KFMLP on our datasets.

We hasten to add that the imaging quality comes at a high computational cost. The FMLP is more expensive to train than the t-DIP and the KFMLP. However, we think that future research (such as pre-training the FMLP) can substantially improve the running time of the FMLP, and different feature encoding altogether might also improve the running time.

A major advantage of the FMLP over the t-DIP and other approaches is its flexibility: To generalized generalize to 3D data, we only need to add an additional spatial input.

Acknowledgements

The authors would like to thank you Kilian Weiss (Philips GmbH Market DACH, Hamburg, Germany) for helpful discussion. The work is supported by the Deutsche Forschungsgemeinschaft (DFG, German Research Foundation) 11 - 456465471, 464123524.

References

- [Ahm+20] A. H. Ahmed, R. Zhou, Y. Yang, P. Nagpal, M. Salerno, and M. Jacob. “Free-Breathing and Ungated Dynamic MRI Using Navigator-Less Spiral STORM”. In: *IEEE Transactions on Medical Imaging* (2020).
- [Ahm+22] A. H. Ahmed, Q. Zou, P. Nagpal, and M. Jacob. “Dynamic Imaging Using Deep Bi-linear Unsupervised Representation (DEBLUR)”. In: *IEEE Transactions on Medical Imaging* (2022).
- [BAJ19] S. Biswas, H. K. Aggarwal, and M. Jacob. “Dynamic MRI Using Model-Based Deep Learning and STORM Priors: MoDL-STORM”. In: *Magnetic Resonance in Medicine* (2019).
- [Chr+18] A. G. Christodoulou, J. L. Shaw, C. Nguyen, Q. Yang, Y. Xie, N. Wang, and D. Li. “Magnetic Resonance Multitasking for Motion-Resolved Quantitative Cardiovascular Imaging”. In: *Nature Biomedical Engineering* (2018).
- [DH21] M. Z. Darestani and R. Heckel. “Accelerated MRI With Un-trained Neural Networks”. In: *IEEE Transactions on Computational Imaging* (2021).

- [Fen+23] J. Feng, R. Feng, Q. Wu, Z. Zhang, Y. Zhang, and H. Wei. *Spatiotemporal Implicit Neural Representation for Unsupervised Dynamic MRI Reconstruction*. 2023. arXiv: [2301.00127](#).
- [Fen+16] L. Feng, L. Axel, H. Chandarana, K. T. Block, D. K. Sodickson, and R. Otazo. “XD-GRASP: Golden-angle Radial MRI with Reconstruction of Extra Motion-State Dimensions Using Compressed Sensing”. In: *Magnetic Resonance in Medicine* (2016).
- [Fen+14] L. Feng, R. Grimm, K. T. Block, H. Chandarana, S. Kim, J. Xu, L. Axel, D. K. Sodickson, and R. Otazo. “Golden-Angle Radial Sparse Parallel MRI: Combination of Compressed Sensing, Parallel Imaging, and Golden-Angle Radial Sampling for Fast and Flexible Dynamic Volumetric MRI”. In: *Magnetic Resonance in Medicine* (2014).
- [HH19] R. Heckel and P. Hand. “Deep Decoder: Concise Image Representations from Untrained Non-convolutional Networks”. In: *International Conference on Learning Representations*. 2019.
- [HS20a] R. Heckel and M. Soltanolkotabi. “Compressive sensing with un-trained neural networks: Gradient descent finds a smooth approximation”. In: *International Conference on Machine Learning*. 2020.
- [HS20b] R. Heckel and M. Soltanolkotabi. “Denoising and Regularization via Exploiting the Structural Bias of Convolutional Generators”. In: *International Conference on Learning Representations*. 2020.
- [Hua+21] W. Huang, Z. Ke, Z.-X. Cui, J. Cheng, Z. Qiu, S. Jia, L. Ying, Y. Zhu, and D. Liang. “Deep Low-Rank plus Sparse Network for Dynamic MR Imaging”. In: *Medical Image Analysis* (2021).
- [Hua+22] W. Huang, H. Li, G. Cruz, J. Pan, D. Rueckert, and K. Hammernik. *Neural Implicit K-Space for Binning-free Non-Cartesian Cardiac MR Imaging*. 2022. arXiv: [2212.08479](#).
- [HA20] R. Hyder and M. S. Asif. “Generative Models for Low-Dimensional Video Representation and Reconstruction”. In: *IEEE Transactions on Signal Processing* (2020).
- [Jia+18] W. Jiang, F. Ong, K. M. Johnson, S. K. Nagle, T. A. Hope, M. Lustig, and P. E. Larson. “Motion Robust High Resolution 3D Free-Breathing Pulmonary MRI Using Dynamic 3D Image Self-Navigator”. In: *Magnetic Resonance in Medicine* (2018).
- [KB17] D. P. Kingma and J. Ba. *Adam: A Method for Stochastic Optimization*. 2017. arXiv: [1412.6980](#).
- [Küs+20] T. Küstner et al. “CINENet: Deep Learning-Based 3D Cardiac CINE MRI Reconstruction with Multi-Coil Complex-Valued 4D Spatio-Temporal Convolutions”. In: *Scientific Reports* (2020).
- [Lan+84] P. Lanzer, E. H. Botvinick, N. B. Schiller, L. E. Crooks, M. Arakawa, L. Kaufman, P. L. Davis, R. Herfkens, M. J. Lipton, and C. B. Higgins. “Cardiac imaging using gated magnetic resonance.” In: *Radiology* (1984).
- [Lar+04] A. C. Larson, R. D. White, G. Laub, E. R. McVeigh, D. Li, and O. P. Simonetti. “Self-Gated Cardiac Cine MRI”. In: *Magnetic Resonance in Medicine* (2004).

- [Mil+22] B. Mildenhall, P. Hedman, R. Martin-Brualla, P. P. Srinivasan, and J. T. Barron. “NeRF in the Dark: High Dynamic Range View Synthesis from Noisy Raw Images”. In: *IEEE/CVF Conference on Computer Vision and Pattern Recognition (CVPR)*. 2022.
- [Mil+20] B. Mildenhall, P. P. Srinivasan, M. Tancik, J. T. Barron, R. Ramamoorthi, and R. Ng. “NeRF: Representing Scenes as Neural Radiance Fields for View Synthesis”. In: *European Conference On Computer Vision*. 2020.
- [Nak+17] U. Nakarmi, Y. Wang, J. Lyu, D. Liang, and L. Ying. “A Kernel-based Low-rank (KLR) Model for Low-dimensional Manifold Recovery in Highly Accelerated Dynamic MRI”. In: *IEEE Transactions on Medical Imaging* (2017).
- [Ong+20] F. Ong, X. Zhu, J. Y. Cheng, K. M. Johnson, P. E. Z. Larson, S. S. Vasanaawala, and M. Lustig. “Extreme MRI: Large-scale Volumetric Dynamic Imaging from Continuous Non-Gated Acquisitions”. In: *Magnetic Resonance in Medicine* (2020).
- [PJ16] S. Poddar and M. Jacob. “Dynamic MRI Using SmooThness Regularization on Manifolds (SToRM)”. In: *IEEE Transactions on Medical Imaging* (2016).
- [Pod+19] S. Poddar, Y. Q. Mohsin, D. Ansah, B. Thattaliyath, R. Ashwath, and M. Jacob. “Manifold Recovery Using Kernel Low-Rank Regularization: Application to Dynamic Imaging”. In: *IEEE Transactions on Computational Imaging* (2019).
- [Qin+19] C. Qin, J. Schlemper, J. Caballero, A. N. Price, J. V. Hajnal, and D. Rueckert. “Convolutional Recurrent Neural Networks for Dynamic MR Image Reconstruction”. In: *IEEE Transactions on Medical Imaging* (2019).
- [Sch+18] J. Schlemper, J. Caballero, J. V. Hajnal, A. N. Price, and D. Rueckert. “A Deep Cascade of Convolutional Neural Networks for Dynamic MR Image Reconstruction”. In: *IEEE Transactions on Medical Imaging* (2018).
- [Seg+10] W. P. Segars, G. Sturgeon, S. Mendonca, J. Grimes, and B. M. W. Tsui. “4D XCAT Phantom for Multimodality Imaging Research”. In: *Medical Physics* (2010).
- [SB06] H. Sheikh and A. Bovik. “Image Information and Visual Quality”. In: *IEEE Transactions on Image Processing* (2006).
- [SPX22] L. Shen, J. Pauly, and L. Xing. “NeRP: Implicit Neural Representation Learning With Prior Embedding for Sparsely Sampled Image Reconstruction”. In: *IEEE Transactions on Neural Networks and Learning Systems* (2022).
- [Sit+20] V. Sitzmann, J. Martel, A. Bergman, D. Lindell, and G. Wetzstein. “Implicit Neural Representations with Periodic Activation Functions”. In: *Advances in Neural Information Processing Systems*. 2020.
- [Tan+20] M. Tancik, P. Srinivasan, B. Mildenhall, S. Fridovich-Keil, N. Raghavan, U. Singhal, R. Ramamoorthi, J. Barron, and R. Ng. “Fourier Features Let Networks Learn High Frequency Functions in Low Dimensional Domains”. In: *Advances in Neural Information Processing Systems*. 2020.
- [UVL20] D. Ulyanov, A. Vedaldi, and V. Lempitsky. “Deep Image Prior”. In: *International Journal of Computer Vision* (2020).
- [VV+22] D. Van Veen et al. “Scale-Agnostic Super-Resolution in MRI Using Feature-Based Coordinate Networks”. In: *Medical Imaging with Deep Learning*. 2022.

- [Wan+04] Z. Wang, A. Bovik, H. Sheikh, and E. Simoncelli. “Image Quality Assessment: From Error Visibility to Structural Similarity”. In: *IEEE Transactions on Image Processing* (2004).
- [Wis+14] L. Wissmann, C. Santelli, W. P. Segars, and S. Kozerke. “MRXCAT: Realistic Numerical Phantoms for Cardiovascular Magnetic Resonance”. In: *Journal of Cardiovascular Magnetic Resonance* (2014).
- [Wu+21] Q. Wu, Y. Li, L. Xu, R. Feng, H. Wei, Q. Yang, B. Yu, X. Liu, J. Yu, and Y. Zhang. “IREM: High-Resolution Magnetic Resonance Image Reconstruction via Implicit Neural Representation”. In: *Medical Image Computing and Computer Assisted Intervention*. 2021.
- [Yoo+21] J. Yoo, K. H. Jin, H. Gupta, J. Yerly, M. Stuber, and M. Unser. “Time-Dependent Deep Image Prior for Dynamic MRI”. In: *IEEE Transactions on Medical Imaging* (2021).
- [Zou+21] Q. Zou, A. H. Ahmed, P. Nagpal, S. Kruger, and M. Jacob. “Dynamic Imaging Using a Deep Generative STORM (Gen-STORM) Model”. In: *IEEE Transactions on Medical Imaging* (2021).

A Ablation Studies of the FMLP

In this section, we conduct ablation studies on the hyperparameters of the FMLP, specifically on the number of hidden layers and neurons per layer of the MLP, and on the spatial and temporal coordinate scales which are important parameters for controlling the spatial and temporal prior imposed on the heart to be reconstructed. We perform grid-searches over those parameters and study the impact on the reconstruction quality and computational costs.

We also study whether the reconstruction quality can be improved by adding an additional loss term that explicitly regularizes the temporal total variation. We find that if the temporal coordinate scale is tuned properly, additional temporal total variation regularization is not beneficial.

The network architecture of the FMLP is critical for performance. We compare two variants of the FMLP with joint and separate Fourier-feature embeddings for the spatial and temporal coordinates. We find that separate embeddings yield an improved reconstruction quality.

All experiments in this section are conducted on the low-resolution high-SNR dataset with $T = 225$ frames corresponding to 4s acquisition length. We train the FMLP until no new SER highscore has been reached in the last 200 epochs and report the performance at the epochs of maximum SER.

For the FMLP, we jointly tune the spatial coordinates s_x and s_y with a fixed ratio. Initially, we intended setting $s_x = s_y$, however, we the field-of-view (FOV) of the experimental datasets is enlarged due to over-sampling along the frequency encoding (k_y) and phase encoding (k_x) dimensions. Thus, we calculated the coordinate grid for a smaller FOV than was actually measured, resulting in new effective coordinate scales with $s_y = 1.43s_x$ in the ablation studies. We find, however, that the skewed coordinate scales yield very similar results to setting $s_y = s_x$.

For simplicity, we define a default hyperparameter configuration for the ablation studies. Unless not stated explicitly, the parameters are set to: spatial coordinate scales $s_y = 1.43s_x = 33 \text{ m}^{-1}$, temporal coordinate scale $s_t = 5.3 \text{ s}^{-1}$, number of lines per frame $N_{\text{lines}} = 6$, number of hidden layers $N_{\text{hidden}} = 7$, and 512 neurons per hidden layer.

A.1 Spatio-temporal coordinate scales regularize the smoothness along spatio-temporal dimensions

The spatio-temporal coordinate scales of the FMLP effectively adjust the regularization strength in the spatial and temporal dimensions. We perform grid-searches over the spatial coordinate scales s_x, s_y and the temporal coordinate scale s_t . For all configurations, we report the maximum SER and the number of training epochs required to reach the maximum SER.

Performance as a function of spatial coordinate scales: Figure 6a shows that the image quality (in SER) as a function of the spatial coordinate scales first improves and then deteriorates, as expected. Too small and too large values result in too little and too much regularization.

Figure 6b shows the number of training epochs required for reaching the maximum SER for different spatial coordinate scales. The figure shows that a smaller number of epochs is required to reach the best SER for a given scale as a function of the spatial coordinate scales. However, for coordinate scales below the threshold of $s_y = 1.43s_x = 2.5 \text{ m}^{-1}$, the number of epochs suddenly decreases. The peculiar decrease may be attributed to the termination policy that stops training once no SER highscore has been achieved within the last 200 epochs. For very low coordinate scales, the convergence is so slow that only small improvements are achieved within 200 epochs. Small

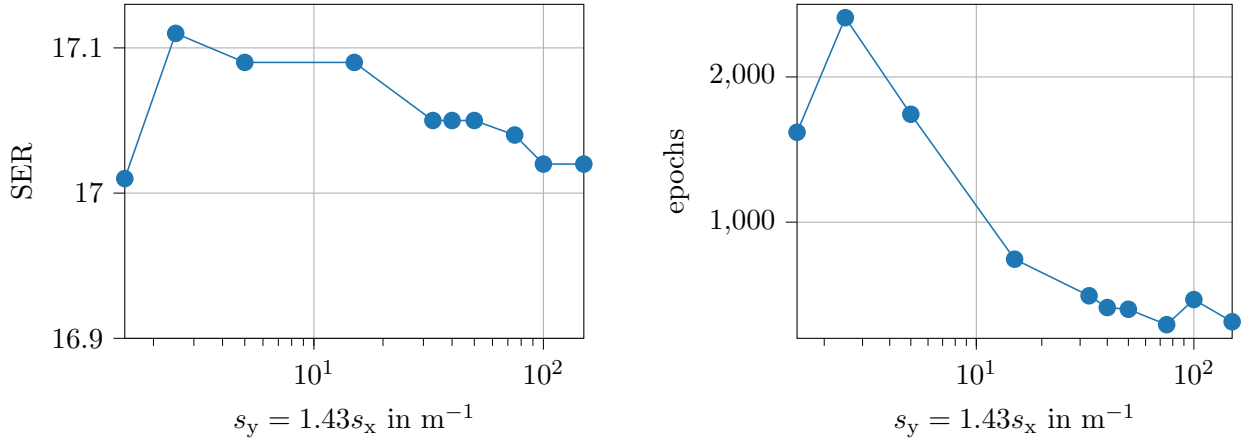
jitters in the SER score cause the training to stop early.

Figure 9 shows images reconstructed at different spatial coordinate scales. It can be seen that lower coordinate scales yield slightly smoother images. The spatial coordinate scales provide control over the smoothness of the reconstructions.

Performance as a function of the temporal coordinate scale: In Figure 7a, the image quality (in SER) is plotted over a range of temporal coordinate scales. The SER reaches its maximum for $s_t = 1 \text{ s}^{-1}$ and gradually decreases for lower and higher spatial coordinate scales. The maximum is reached for relatively low temporal coordinate scales, indicating that strong regularization along the temporal dimension is beneficial for reconstruction quality. For very low temporal coordinate scales, the implicit bias of the network towards slow temporal changes becomes so strong that the SER decreases.

Figure 7b presents the number of training epochs to reach the maximum SER as a function of the temporal coordinate scale. Similar to the trend observed for spatial coordinate scales, the number of epochs increases as the temporal coordinate scale decreases.

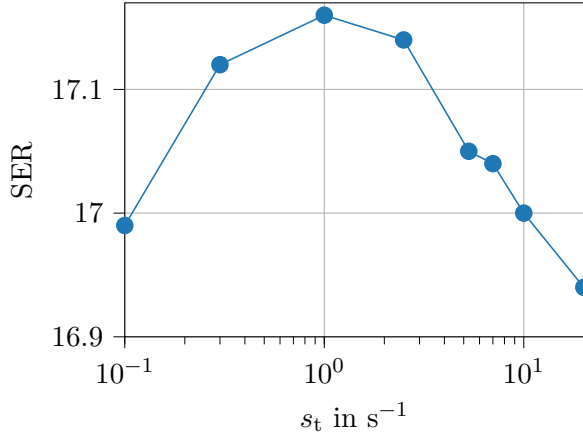
Figure 8a shows how the temporal coordinate scale controls the smoothness of the reconstruction in the temporal dimensions. It plots the average pixel intensity over time within a small image patch that does not contain moving body parts. For low temporal coordinate scales, the average pixel intensity varies smoothly over time, whereas for large scales, e.g., $s_t = 20 \text{ s}^{-1}$, the average pixel intensity is fluctuating rapidly. The fluctuations can also be seen in the reconstructed video as flickering. The flickering may be caused by the sampling pattern of the low-resolution high-SNR dataset. The image contrast is predominantly contained around the k-space origin that is sampled only in some frames. Thus, the contrast information in the measurement data varies over the frames.



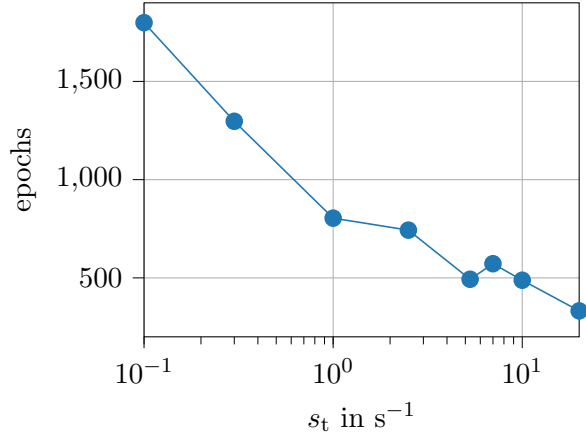
(a) The image quality (in SER), as a function of the spacial coordinate s_y , which is coupled to the scale s_x as $s_y = 1.43s_x$. It can be observed that the SER increases as the spatial coordinate scales decrease, until the SER drops for very low coordinate scales, e.g., $s_y = 1.43s_x = 1.5 \text{ m}^{-1}$.

(b) The number of training epochs as a function of the spatial coordinate scales $s_y = 1.43s_x$. The number of epochs increases for decreasing spatial coordinate scales until a threshold. Below the threshold, the number of epochs drops. The drop is may be caused by the slow convergence and the stopping criterion that stops training after 200 epochs without new SER highscore.

Figure 6: Choosing the spatial coordinate scales s_x, s_y is a trade-off between SER and training time.



(a) The image quality measured by the SER is plotted over a range of temporal coordinate scales. Among the tested configurations, the SER reaches its maximum for $s_t = 1 s^{-1}$ and drops for lower and higher scales.



(b) The number of epochs is shown as a function of the spatial coordinate scale. It increases as the temporal coordinate scale is decreased.

Figure 7: The temporal coordinate scale s_t affects the maximum SER and the training time.

A.2 Network size: number of layers and layer width

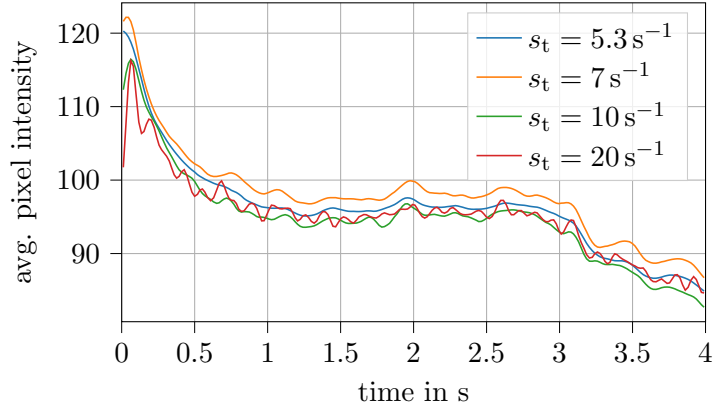
The MLP’s network size is a critical parameter that affects the reconstruction quality and training time. In this section, we perform an ablation study on the number of hidden layers N_{hidden} and the number of neurons per hidden layer. The reported training time is measured by the wall clock time and thus includes data-loading, logging, and computation of the SER after every epoch.

Performance as a function of the number of hidden layers: We train models with different numbers of hidden layers and measure SER, training time, and number of epochs. Figure 10a shows that on this dataset, the SER increases in increasing the number of layers in the range from 3 to 9 layers.

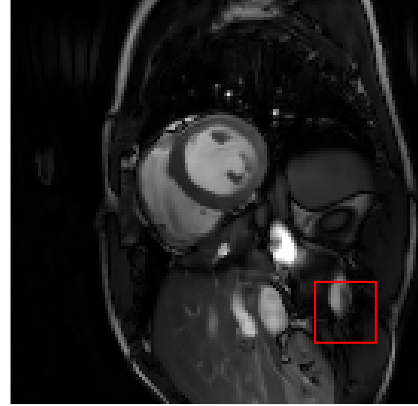
However, an increased number of hidden layers comes at the cost of a longer training time per epoch as can be seen by the slope of the gray lines in Figure 10b that displays the training time vs. number of epochs for different parameter configurations of N_{hidden} . The shortest training time is achieved for a relatively small number of hidden layers, i.e., $N_{\text{hidden}} = 5$. For more hidden layers, i.e., $N_{\text{hidden}} > 5$, the number of epochs and the training time per epoch increases. For fewer hidden layers, the number of epochs increases substantially, eliminating the benefit of the decreased training time per epoch.

Performance as a function of the number of neurons per hidden layer: We now consider the number of neurons per hidden layer and report the SER, training time, and the number of epochs. In Figure 11a, the SER is plotted as a function of the number of neurons per hidden layer. The maximum SER is achieved for a relatively low number of neurons (256) and slightly decreases for increasing number of neurons. For fewer neurons, i.e., 128, the SER declines rapidly, presumably as the network can no longer fit the target signal.

Figure 11b shows the training time and the number of epochs for different numbers of neurons per layer. As expected, the training time per epoch increases in the number of neurons. The shortest



(a) The graphs are obtained by averaging the pixel intensities within the image patch shown in Figure 8b. The plot shows that the value of the temporal coordinate scale s_t affects the smoothness of pixel intensities over time. Hence, the regularization strength along the temporal dimension can be adjusted by the temporal coordinate scale.



(b) For Figure 8a, we average the pixel intensity of the image patch marked in red. The patch is chosen from a region that is not notably affected by the cardiac and respiratory motion.

Figure 8: The temporal coordinate scale s_t affects the temporal smoothness and acts as a regularization parameter for temporal changes.

overall training time is achieved for 384 neurons per layer, i.e., for moderate numbers of neurons. For an increased number of neurons, the longer training time per epoch mainly affects the overall training time. For fewer neurons, the increased number of epochs compensates the benefits of the decreased training time per epoch.

A.3 Explicit temporal TV regularization

We study if the reconstruction quality of the FMLP can be improved by adding an additional loss term that explicitly regularizes the temporal relation by imposing a total variation (TV) norm penalty. We find that such regularization does not notably improve the image quality if the temporal coordinate scale is tuned properly.

For the experiment, we add a TV norm penalty to the training loss

$$\mathcal{L}(\theta) = \frac{1}{T} \sum_{\tau=1}^T \|\mathbf{A}_\tau \mathbf{f}_\theta(t_\tau) - \mathbf{y}_\tau\|_2^2 + \lambda_{\text{TV}} \mathcal{L}_{\text{TV},\tau}(\theta),$$

where $\mathcal{L}_{\text{TV},\tau} > 0$ is a hyperparameter that adjusts the regularization strength, and the total-variation loss is defined as follows. We compute the temporal TV loss between the current reconstruction $\mathbf{f}_\theta(t_\tau)$ and the latest reconstructions $\hat{\mathbf{x}}_i$, $i = 1, \dots, T$ that are stored from an earlier training epoch or from an earlier iteration within the current epoch. The batch-size is set to 1, meaning that gradients are computed for individual frames. The gradient of the loss is only computed with respect

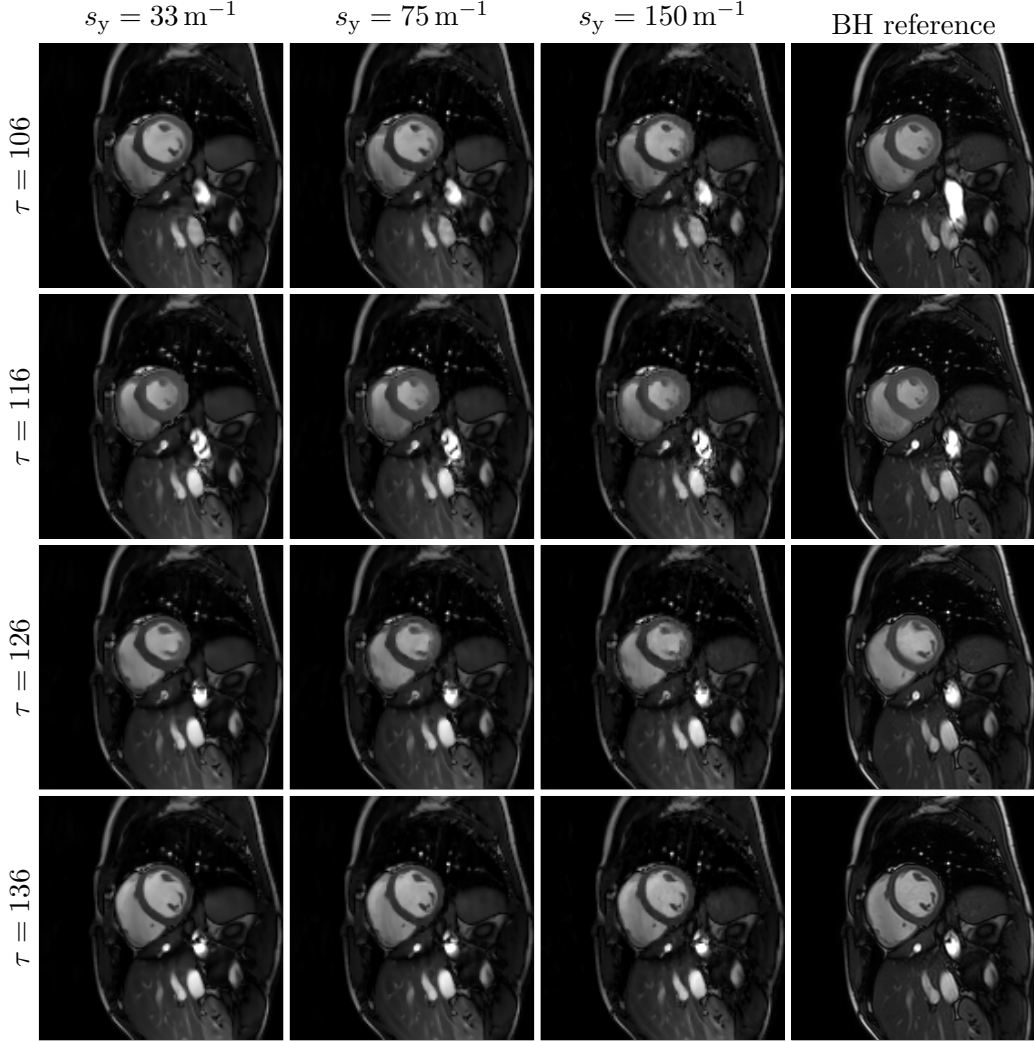


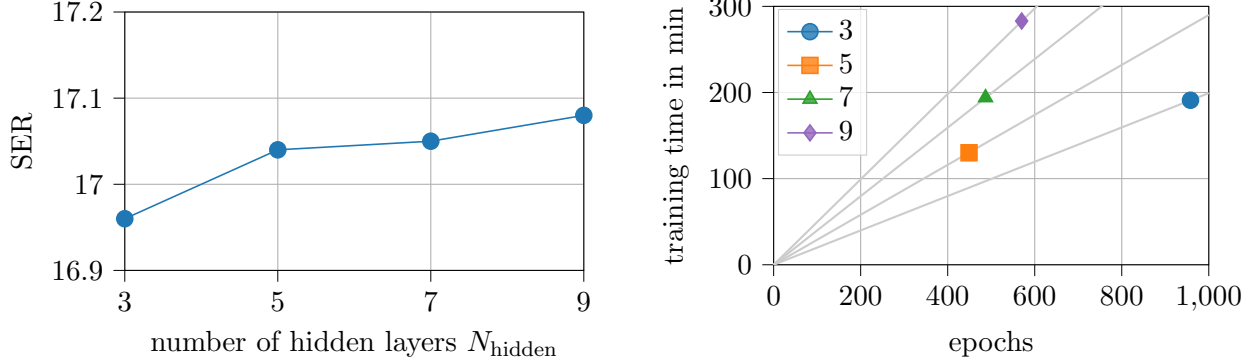
Figure 9: Reconstructions are shown for different spatial coordinate scales. The smaller the coordinate scales, the smoother the image is. The spatial coordinate scales s_x and s_y control the regularization along the spatial dimensions.

to the current reconstruction $\mathbf{f}_\theta(t_\tau)$. The loss computes as

$$\mathcal{L}_{\text{TV},\tau}(\theta) = \begin{cases} \|\mathbf{f}_\theta(t_1) - \hat{\mathbf{x}}_2\|_1, & \tau = 1, \\ \|\mathbf{f}_\theta(t_\tau) - \hat{\mathbf{x}}_{\tau-1}\|_1 + \|\mathbf{f}_\theta(t_\tau) - \hat{\mathbf{x}}_{\tau+1}\|_1, & \tau < 1 \wedge \tau < T, \\ \|\mathbf{f}_\theta(t_T) - \hat{\mathbf{x}}_{T-1}\|_1, & \tau = T, \end{cases}$$

where the l_1 norm is computed for the real and imaginary part separately and is added.

Figure 12 shows the reconstruction quality as measured by the SER as a function of the hyperparameter λ_{TV} for different choices of the temporal coordinate scale s_t . It can be seen that the SER does not improve notably for regularization strength beyond $\lambda_{\text{TV}} = 0$ (no regularization), when the implicit regularization is sufficiently well tuned. Therefore, additional TV regularization is not recommended in the optimized operating regime of the FMLP.



(a) The FMLP’s image quality in terms of the SER is displayed for different numbers of hidden layers N_{hidden} . Within the examined range, the SER generally improves with more hidden layers.

(b) The training time as measured by the wall-clock time is plotted vs. the number of epochs for different numbers of hidden layers N_{hidden} . The slope of the gray lines indicates the training time per epoch. The number of epochs until the maximum SER is reached is minimized for $N_{\text{hidden}} = 5$. Both the training time and the number of epochs increase for fewer or more hidden layers.

Figure 10: Reconstruction quality in SER a training time as a function of the number of hidden layers N_{hidden} . The experiments are conducted with 512 neurons per layer.

A.4 Separate spatial and temporal Fourier-feature embeddings yields sharper images

Our proposed network architecture uses separate Fourier-feature embeddings for the spatial coordinates and the temporal coordinate. An alternative is to jointly embed the spatial and temporal coordinates. In this section, we compare the performance of FMLP with separate and joint embeddings.

As before, the separate embedding is as explained in Section 4 in the main body. For the joint embedding, the spatio-temporal coordinate vector is embedded in the 640 dimensional feature vector

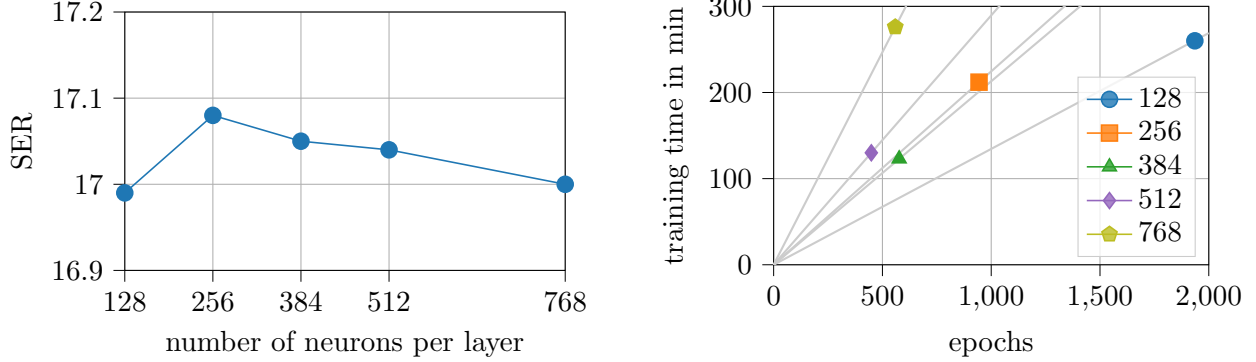
$$\gamma_{\text{joint}}([x, y, t]) = \left[\sin \left(\tilde{\mathbf{B}} \begin{bmatrix} s_x x \\ s_y y \\ s_t t \end{bmatrix} \right), \cos \left(\tilde{\mathbf{B}} \begin{bmatrix} s_x x \\ s_y y \\ s_t t \end{bmatrix} \right) \right]^T,$$

where the elements in the matrix $\tilde{\mathbf{B}} \in \mathbb{R}^{320 \times 3}$ are drawn independently from the standard normal distribution. The coordinate scales are set to the their default values for both configurations.

Our results show that the image quality in terms of the SER drops from 17.05 to 16.76 if the coordinates are embedded jointly. The difference is also visible in Figure 13, where separating embeddings of the spatial and temporal coordinates yield sharper reconstructions than joint embeddings.

A.5 Temporal resolution of the binning into frames

Our measurement model in Section 3 is based on the assumption that the heart is essentially static during a frame. However, even though the frame duration is very small, the heart is moving



(a) The image quality in terms of the SER is plotted for different numbers of neurons per hidden layer. The SER is maximized for 256 neurons per hidden layer. The performance sharply declines for fewer neurons per layer and degrades slowly for an increased number of neurons per layer.

(b) The training time and the number of epochs are shown for different numbers of neurons per hidden layer. As expected, the training time per epoch increases with the number of neurons per hidden layer (slope of the gray lines), except for the outlier at 256 neurons per layer. The maximum SER is reached with the least amount of training time for 384 neurons per layer.

Figure 11: Effects of changing the number of neurons per hidden layer. For the experiment, the number of hidden layers is set to $N_{\text{hidden}} = 5$.

continuously while measurements are taken sequentially. The longer the frame, the more the heart moves during the frame, and the larger the error in assuming the heart is constant. In this section, we perform an ablation study over the duration of frames, i.e., the temporal resolution of the binning and study if the image quality improves when improving the temporal resolution.

The temporal resolution is determined by the number of measured k_y -lines N_{lines} that are binned together in a frame. We train the FMLP on datasets with different N_{lines} , ranging from 4 to 36 and report the image quality as measured by the SER and the training time. Note that we change the temporal resolution of the frames without significantly changing the amount of training data. As we increase the number of lines per frame, the number of frames is decreased, such that the total number of measurements stays approximately constant at $225 \cdot 6 = 1350$ lines. We extract the same lines for validation across all temporal resolutions such that the SER values can be compared across temporal resolutions.

Figure 14a shows that the SER improves as the number of measured k-space lines per frame N_{lines} decreases, which is equivalent to increasing the temporal resolution. The result is to be expected as the mismatch between the true measurement process and our measurement model is reduced by decreasing N_{lines} . With increased temporal resolution, the motion within a frame is reduced. Increasing the temporal resolution, however, comes at the cost of longer training time as the model has to be trained on more frames per epoch, see Figure 14b.

B Ablation Studies of the KFMLP

We perform ablation studies on several of the KFMLP’s hyperparameters including the spatial coordinate scales s_x, s_y , the output scale s_{out} of the network, the hyperparameter ϵ of the high-

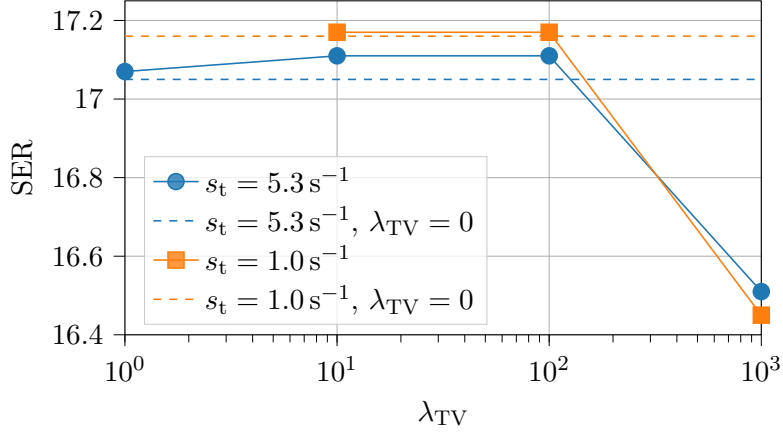


Figure 12: The image quality as measured by the SER is plotted for different choices of the hyperparameter λ_{TV} that controls the strength of the explicit TV regularization. The explicit temporal TV regularization improves the SER for higher spatial coordinate scales, i.e., weak implicit regularization. If the implicit regularization is stronger, i.e., for lower coordinate scales, the SER does not improve much by regularizing explicitly. For both scenarios, the SER drops rapidly if the explicit temporal regularization is too strong.

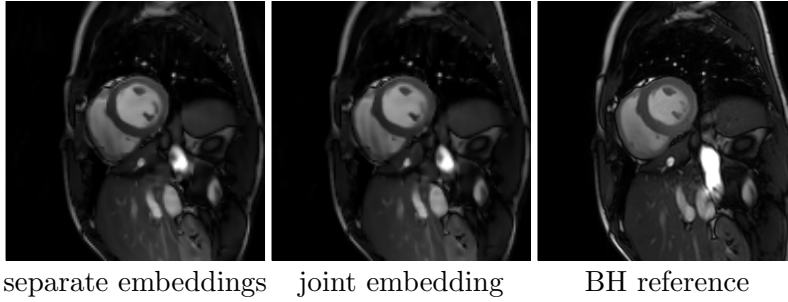
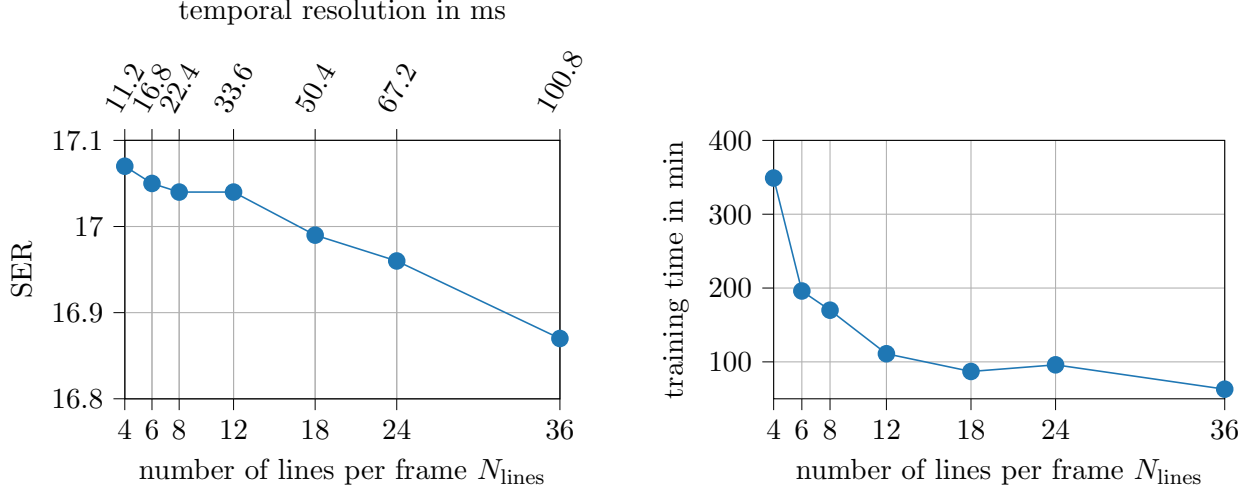


Figure 13: Reconstructions by the FMLP are shown for architectures with separate and joint embedding of the spatial and temporal coordinates, alongside with a reconstruction of the low-resolution high-SNR dataset breath-hold dataset that serves as visual reference. The architecture with separate coordinate embeddings yields an improved image quality with sharper details compared to the architecture with a joint embedding. The reconstructions are shown for frame $\tau = 106$.

dynamic-range loss, and the hyperparameters $\lambda_{\text{denoiser}}$ and σ of the k-space denoiser. The ablation studies are conducted on the low-resolution high-SNR dataset. The KFMLP is trained until no new SER high-score has been achieved in the last 200 epochs. A total of $T = 225$ frames of data are used for the reconstruction with 6 k_y -lines per frame. It is important to note that the bin size does not directly affect the temporal resolution of the reconstructions since the KFMLP can be fitted at the exact temporal coordinates without binning. However, the number of k_y -lines per frame is the equivalent of a batch-size, and therefore affects the computational speed.

For brevity, we define a default hyperparameter configuration. Unless not stated explicitly, the hyper-parameters are: $s_{\text{out}} = 1000$, $s_t = 1.0 \text{ s}^{-1}$, $s_x = s_y = 10$, 7 hidden layers with 512 neurons per layer.



(a) The FMLP is trained on datasets with binnings of different temporal resolutions, i.e., different number of lines per frame N_{lines} , and the SER is computed on a validation dataset that is kept constant for all temporal resolutions. The figure shows that the image quality improves with increased temporal resolution, i.e., lower N_{lines} .

(b) The training time measured by the wall-clock time is reported for different temporal resolutions, i.e., different numbers of k_y -lines per frame. The training time increases with decreasing N_{lines} due to the increasing number of frames T that need to be processed in each epoch.

Figure 14: Increasing the temporal resolution of the frames improves the maximum SER but comes at the cost of increased training time.

B.1 SER is sensitive to the choice of the spatial coordinate scales

The spatial coordinate scales s_x and s_y affect the implicit bias of the network towards low-frequency signals and need to be tuned carefully. In this section, we perform a grid search over the spatial coordinate scales $s_x = s_y$ and measure the achieved reconstruction quality in SER. The experiment is repeated for different output scales s_{out} . The experiment is conducted with the following l_2 reconstruction loss instead of the high-dynamic-range loss, and without the k-space denoiser.

$$\mathcal{L}(\theta) = \frac{1}{T} \sum_{\tau=1}^T \left\| f_{\theta, \tau}^{\text{traj}} - \mathbf{y}_{\tau} \right\|_2^2$$

By first evaluating the performance using the l_2 loss we establish a baseline for comparing the performance to the high-dynamic-range loss. Figure 15 illustrates the SER values obtained for different spatial coordinate scales. The figure demonstrates that the KFMLP’s reconstruction performance is significantly affected by variations in spatial coordinate scales. Among the tested configurations, the maximum SER is achieved for $s_x = s_y = 10$ and declines rapidly for lower and higher coordinate scales. Thus, careful tuning is necessary to ensure good performance.

B.2 High-dynamic-range reconstruction loss improves the SER marginally

In this section, the KFMLP is trained using the HDR reconstruction loss and an ablation study on the hyperparameter ϵ of the HDR loss is performed. The k-space denoiser is disabled by setting

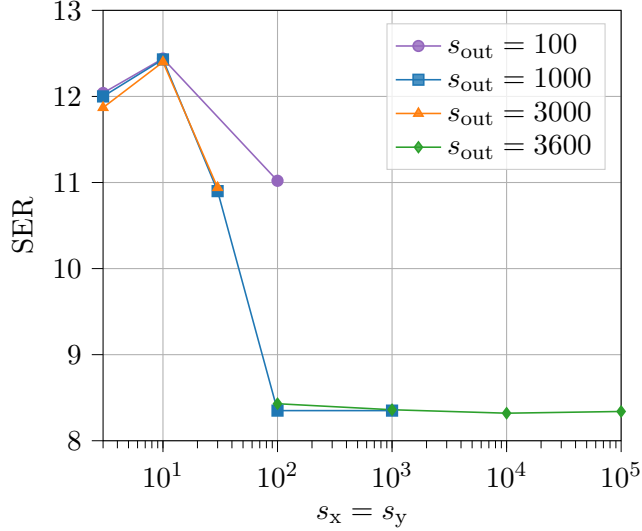


Figure 15: An ablation study of the KFMLP’s spatial coordinate scales and the output scale s_{out} is conducted. The standard l_2 reconstruction loss is used and the k-space denoiser is deactivated by setting $\lambda_{denoiser} = 0$. The image quality is reported in terms of the SER. The highest SER scores are achieved for relatively low spatial coordinate scales with a sharp maximum at around $s_x = s_y = 10$.

$\lambda_{denoiser} = 0$. Thereby, the performance of the KFMLP with HDR loss can be compared to the performance with the l_2 reconstruction loss that was used in the previous Section B.1. The study is repeated for two different spatial coordinate scales $s_x = s_y = 3$ and $s_x = s_y = 10$.

Figure 16 shows the image quality measured by the SER as a function of the hyperparameter ε . For comparison, the SER with the l_2 reconstruction loss is included in the graph. The HDR loss improves the SER only marginally compared to the standard l_2 reconstruction loss. If ε is not tuned properly, however, the HDR loss degrades the reconstruction quality. Thus, using the HDR loss is only advisable if ε can be tuned carefully.

B.3 K-space denoiser improves the SER marginally

In the last section, the KFMLP’s hyperparameters were optimized with a disabled k-space denoiser. In this section, the k-space denoiser is enabled and an ablation study of the the denoiser’s hyperparameters $\lambda_{denoiser}$ and σ is conducted.

Figure 17 shows the SER as a function of σ controlling the decay of the weights in the filter matrix \mathbf{K} . The experiment is conducted for different regularization strengths $\lambda_{denoiser}$. The figure demonstrates that the k-space denoiser improves the SER if the hyper-parameters $\lambda_{denoiser}$ and σ are tuned properly. However, the improvements are small and are only achieved for a precise tuning of the hyperparameters.

C Experiments on Phantom Data

It is common practice to measure the image quality with full-reference image quality metrics. However, the required reference images are not available for the datasets used in our other experiments. Thus,

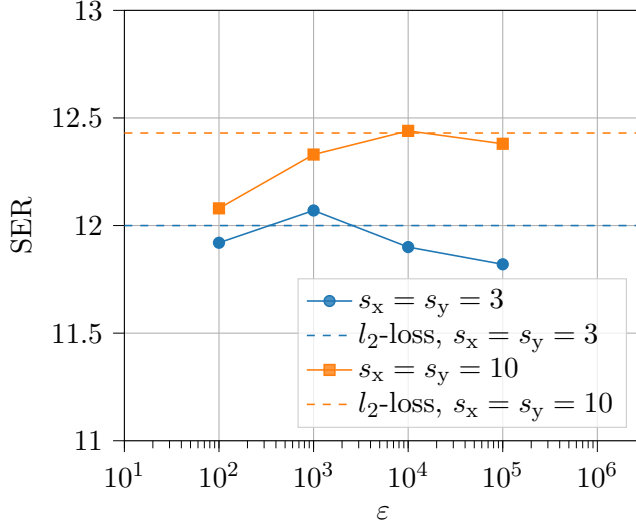


Figure 16: The KFMLP’s image quality in terms of the SER is shown for a different choices of the hyperparameter ε that adjusts the compression of the dynamic range. For comparison, the results of the KFMLP with l_2 reconstruction loss are included. The figure shows that the HDR loss slightly improves the SER compared to the l_2 loss if ε is tuned properly. If not tuned properly, the HDR loss performs worse than the standard l_2 loss.

we conduct additional experiment on phantom data, where ground-truth images are available.

C.1 Phantom dataset

We generated a phantom dataset with MRXCAT [Wis+14], a numerical phantom that can simulate cardiac and respiratory motion. It computes synthetic MR images from body slices of the 4D cardiac-torso phantom XCAT [Seg+10]. The synthetic images are passed through the imaging equation (1) to obtain synthetic k-space data.

We generate datasets with the exact same sampling masks \mathbf{M}_τ as for the experimental low-resolution datasets. Each measured k-space line is synthesized from an individual image in a different motion state to imitate the sequential sampling of k-space coordinates.

C.2 Comparison of the methods by evaluating full-reference image quality metrics

The FMLP, KFMLP, and the t-DIP are evaluated on the phantom dataset and the full reference image quality metrics SSIM and VIF are computed using the ground-truth images that are available for the phantom dataset. The results are reported in Table 3. We find that the FMLP achieves marginally higher SSIM and VIF scores on the phantom dataset than the t-DIP. The SER, by contrast, is slightly higher for the t-DIP than for the FMLP. The differences are small and the two methods give similar reconstruction quality. The KFMLP achieves much lower SER, SSIM, and VIF scores than FMLP and t-DIP.

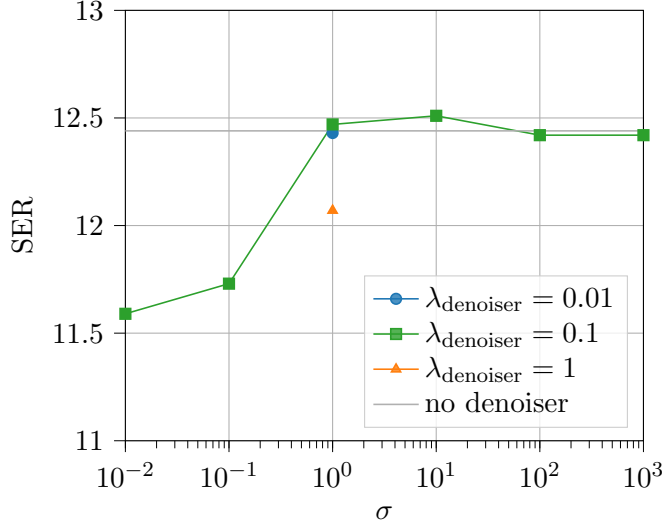


Figure 17: The KFMLP’s image quality measured by the SER is plotted for different configurations of the k-space denoiser’s hyperparameters σ and $\lambda_{\text{denoiser}}$. For comparison the performance with disabled k-space denoiser ($\lambda_{\text{denoiser}} = 0$) is included in the graph. The figure shows that the k-space denoiser slightly improves the maximum SER of the KFMLP but not by a substantial margin.

metric	FMLP	KFMLP	t-DIP
max. SER	23.70	12.73	23.74
SSIM at max. SER epoch	0.986	0.126	0.973
VIF at max. SER epoch	0.694	0.120	0.682

Table 3: The performance metrics are evaluated on the phantom dataset. The t-DIP achieves a higher data consistency according to the SER, however, the FMLP slightly outperforms the t-DIP in the image quality metrics SSIM and VIF. The KFMLP achieves much lower SER, SSIM, and VIF scores. The models were trained on $T = 225$ frames.

D Reconstructed Images at Full Resolution

The reconstructions shown in Section 5 are truncated to the region-of-interest, the heart. For completeness, the reconstructions are shown with a larger field-of-view in Figures 18, 19, and 20 for the low-resolution high-SNR, the low-resolution low-SNR, and the high-resolution dataset, respectively.

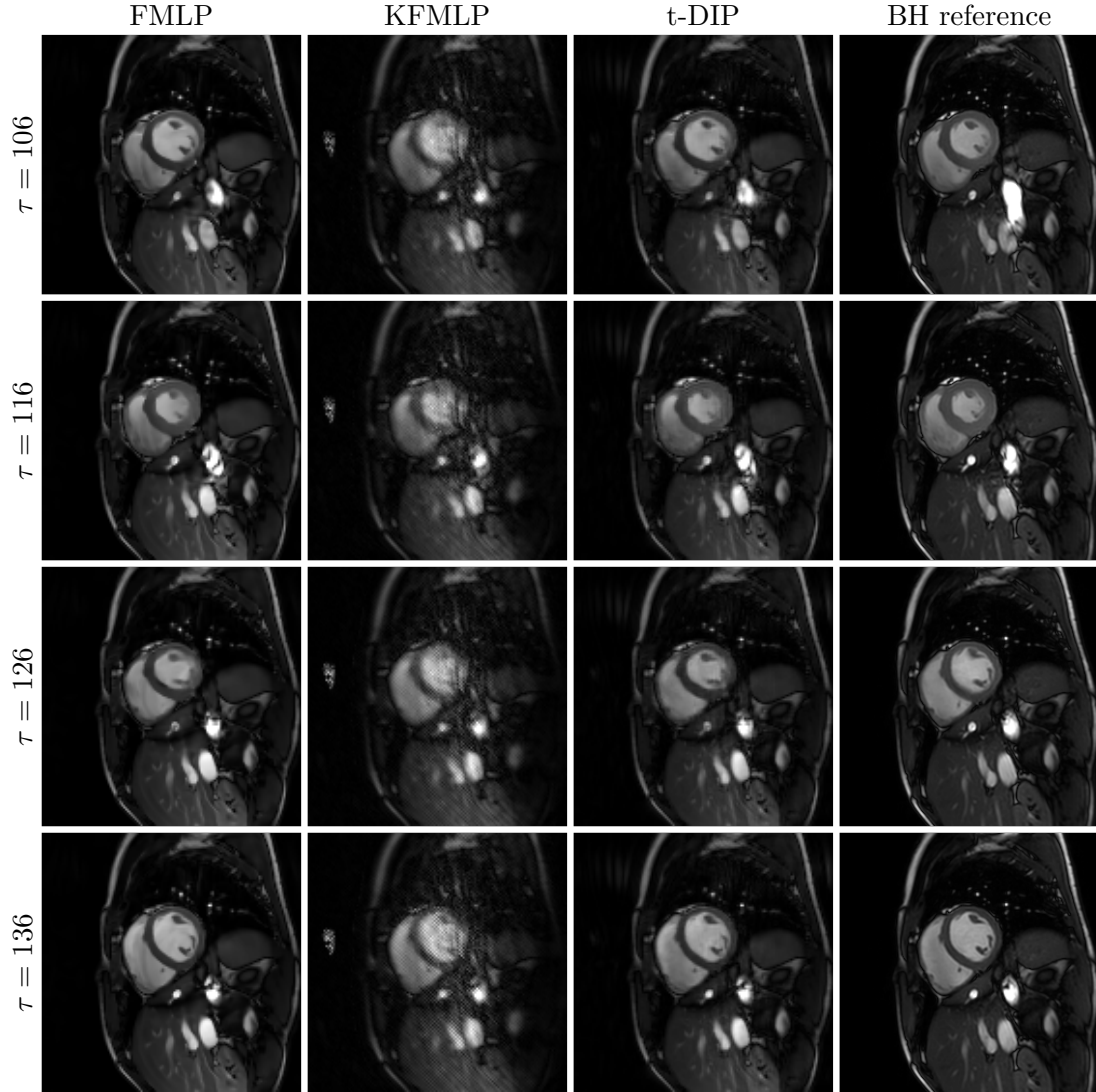


Figure 18: The reconstructions of the low-resolution high-SNR dataset of Figure 3 are shown with a larger field-of-view. It can be seen that the FMLP and the t-DIP achieve a similar reconstruction quality whereby the FMLP recovers small anatomic details in the heart, such as the papillary muscles, more accurately. The KFMLP, by contrast, suffers from aliasing-like artifacts.

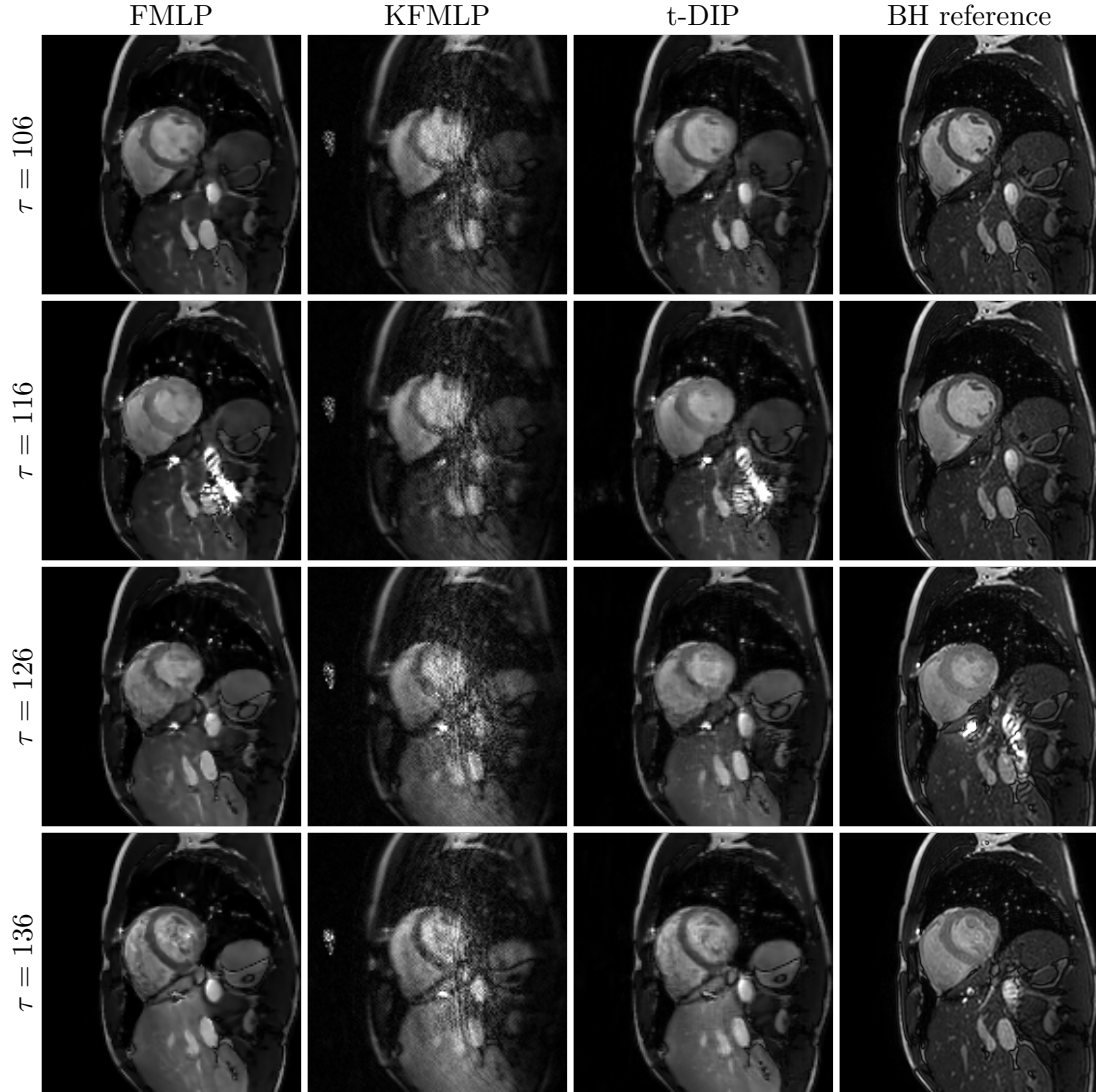


Figure 19: The reconstructions of the low-resolution low-SNR dataset of Figure 4 are shown with a larger field-of-view. The figure shows that the FMLP and the t-DIP exhibit similar artifacts and are on par in terms of image quality. The KFMLP, however, has a low image quality with aliasing-like artifacts and noise superimposed on the image. The artifacts are most prominent in the center of the image around the heart where the motion is strongest.

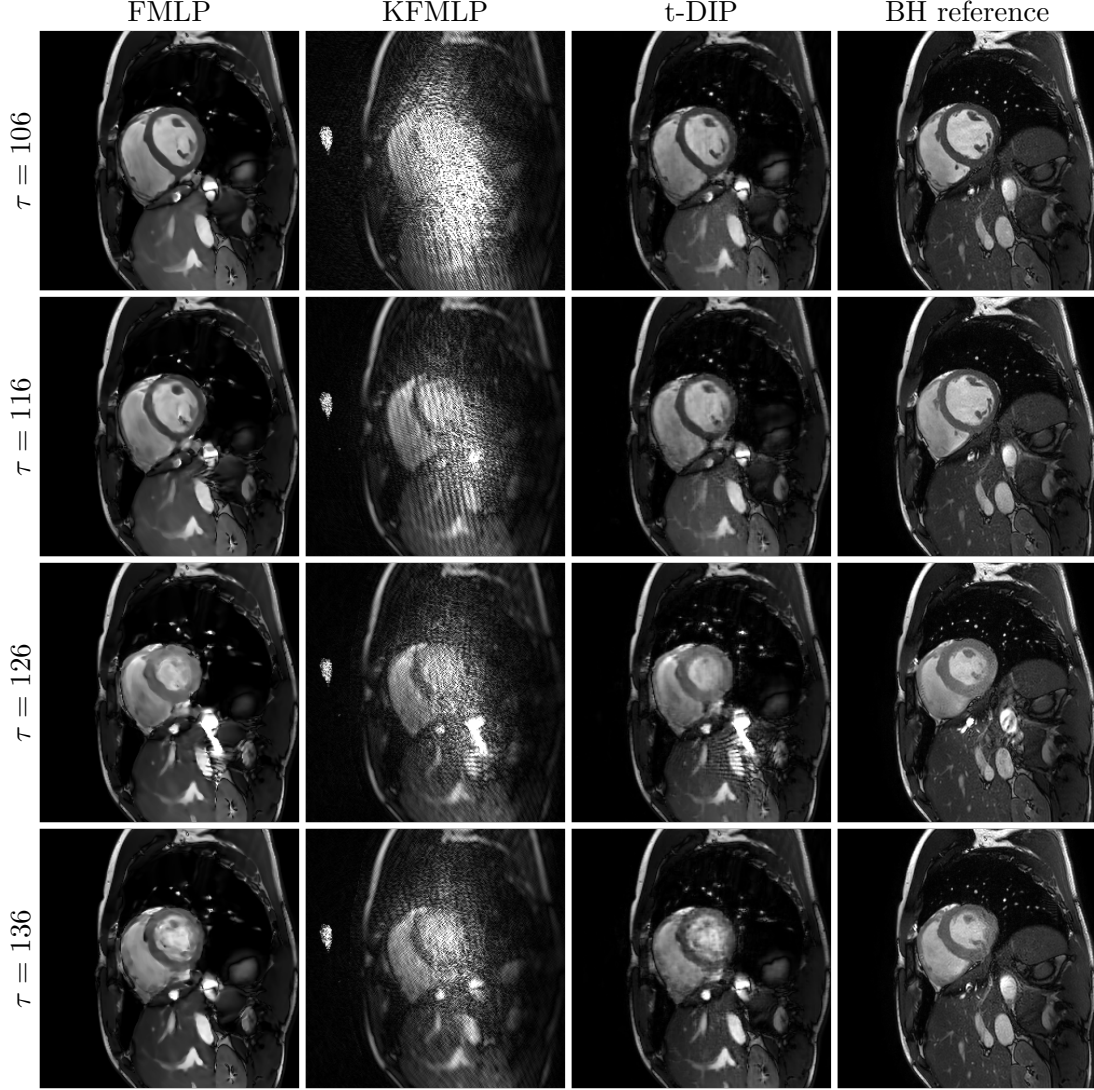


Figure 20: The reconstructions of the high-resolution dataset of Figure 5 are shown with a larger field-of-view. The image quality of the FMLP and the t-DIP are similar, whereas the KFMLP’s reconstructions are distorted by noise that obscures meaningful anatomic details in the heart.

E Measurement Parameters of the Datasets

The experimental datasets were acquired with a 2D balanced steady-state free precession (SSFP) sequence using a flip angle of 45° on a 3 T Elition X scanner (Philips Healthcare, The Netherlands). The free-breathing (FB) scans are taken with $C = 25$ active receiver coils, while the breath-hold (BH) scans use a total of $C = 26$ receiver coils. The free-breathing datasets are recorded with a partial-Fourier deterministic sampling pattern that cover 62.5 % of the k-space in phase-encoding (k_y) direction. The pattern of the low-resolution datasets is illustrated in Figure 21. Further parameters of the free-breathing datasets are listed in Table 4. The breath-hold scans are sampled using a SENSE sampling pattern with an acceleration factor of $R = 2$ and 40 dynamics per cardiac

cycle. For further details see Table 5.

Experiment	low resolution, high-SNR	low resolution, low-SNR	high resolution
Slice thickness [mm]	10	2.25	5
Field-of-view [mm ²]	600 x 420	600 x 420	600 x 420
Acquisition matrix size	264 x 186	264 x 186	480 x 334
TR / TE [ms]	2.8 / 1.39	3.5 / 1.76	3.4 / 1.71

Table 4: Experiment-specific sequence parameters of the free-breathing scans.

Experiment	low resolution, high-SNR	low resolution, low-SNR	high resolution
Slice thickness [mm]	10	2.25	5
Field-of-view [mm ²]	600 x 540	600 x 540	600 x 330
Acquisition matrix size	264 x 240	264 x 240	480 x 264
TR / TE [ms]	2.8 / 1.38	3.5 / 1.75	3.5 / 1.77
TFE factor / shots / interval [ms]	16 / 5 / 44.2	12 / 6 / 41.9	12 / 11 / 42.4

Table 5: Experiment-specific sequence parameters of the breath-hold scans.

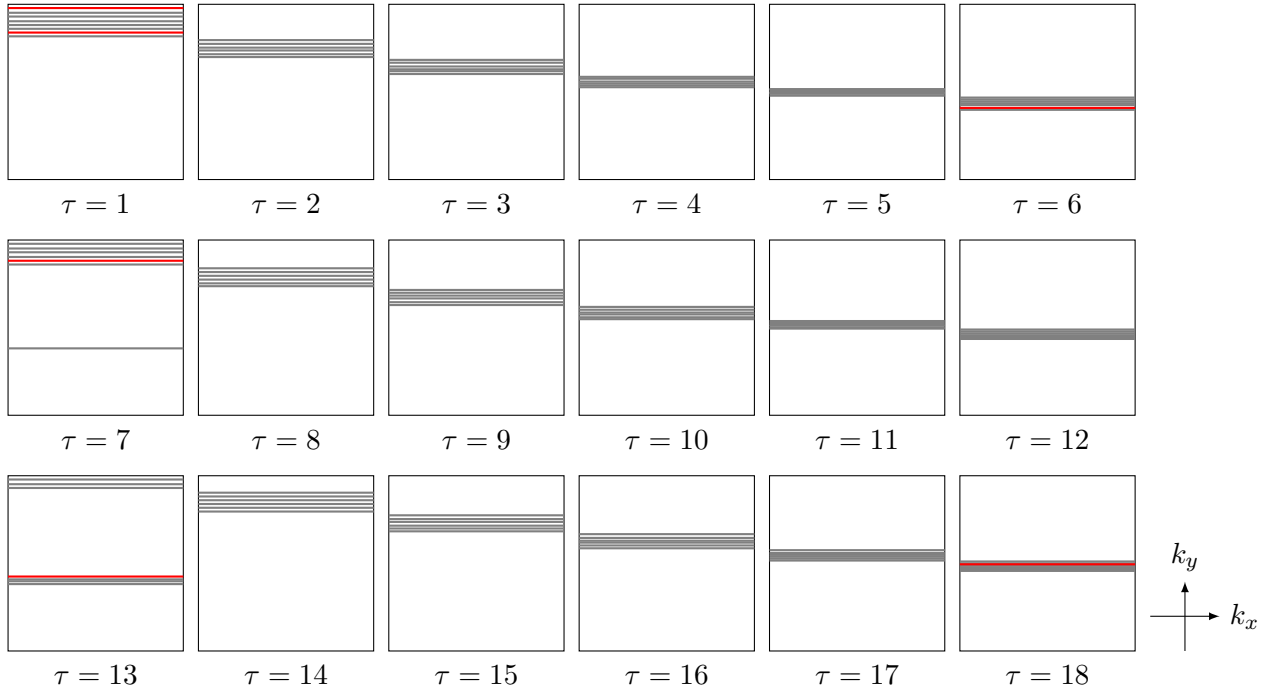


Figure 21: The sampling masks of the first 18 frames are illustrated for the low-resolution datasets with a binning into six lines per frame. The six k_y -lines that are used for training are colored in gray and the randomly selected validation lines are colored in red. The k_y -lines are measured in descending order from positive to negative k_y -coordinates. Due to the sampling pattern, validation lines are always in proximity of lines that are part of the training dataset.